https://doi.org/10.5194/acp-2021-100
Preprint. Discussion started: 25 February 2021

Atmospheric Chemistry and Physics Discussions

Observational study for strong downslope wind event under fine weather condition during ICE-POP 2018

Chia-Lun Tsai[1], Kwonil Kim[1], Yu-Chieng Liou[2], Jung-Hoon Kim[3] , YongHee Lee[4], and GyuWon Lee*[1]

[1]Department of Astronomy and Atmospheric Sciences, Center for Atmospheric REmote sensing (CARE), Kyungpook National University, Daegu, Korea

[2]Department of Atmospheric Sciences, National Central University, Jhongli, Taiwan

[3]School of Earth and Environmental Sciences, Seoul National University, Seoul, Korea

[4]Numerical Modeling Center (NMC), Korea Meteorological Administration, Seoul, Korea

* Corresponding author: Prof. GyuWon Lee, E-mail: gyuwon@knu.ac.kr

https://doi.org/10.5194/acp-2021-100
Preprint. Discussion started: 25 February 2021

Atmospheric Chemistry and Physics Discussions

Abstract

A strong downslope wind event under fine weather condition on 13–15 February 2018 was examined by various observational and high resolution reanalysis datasets during the 2018 Winter Olympic and Paralympic games in Pyeongchang, Korea. High spatio-temporal resolution of wind information was obtained by Doppler lidars, automatic weather stations (AWS), wind profiler, and sounding observations under the International Collaborative Experiments for Pyeongchang 2018 Olympic and Paralympic winter games (ICE-POP 2018). This study aimed to understand the possible generation mechanisms of localized strong wind event across high mountainous areas and in the lee side of mountains associated with the underlying large-scale pattern of a low-pressure system (LPS). The spatial distribution of linear trends for surface wind shows different patterns, exhibiting increased trend in the lee side and a persistent one in mountainous areas with the approaching LPS. Surface wind speed was intensified dramatically from ~3 to ~12 m s^{-1} (gust was stronger than 20 m s^{-1} above ground) at a surface station in the lee side (named as GWW). However, the mountainous station at DGW site appeared to have a persistently strong wind (~10 m s^{-1}) during the research period. Budget analysis of horizontal momentum equation and local reanalysis data suggests that the pressure gradient force (PGF) derived by adiabatic warming along the downslope and subsequent hydraulic jump in the lee side of mountains was a main factor in the acceleration of the surface wind at the GWW site. Detailed analysis of the retrieved 3D winds reveals that the PGF also dominate at the DGW site, which causes the persistent strong wind that is related to the channeling effect across the valley areas in the mountain range. The observational evidence presented here shows that the different mechanisms in local areas under the same synoptic condition with LPS are important references in determining the strength and persistence of the orographic-induced strong winds under fine weather condition.

https://doi.org/10.5194/acp-2021-100
Preprint. Discussion started: 25 February 2021


Atmospheric Chemistry and Physics Discussions

1 Introduction

In mountain regions, wind is an important atmospheric phenomena as enhanced precipitation may be usually caused by the wind impinging topography (Medina et al., 2007; Yu and Cheng, 2008; Panziera and Germann, 2010; Houze, 2012; Yu and Tsai, 2017; Tsai et al., 2018). Therefore, topography could significantly affect the behavior of winds to accelerate the wind speed or to change the wind direction. Such orographically strong wind and mountain waves can highly induce huge impacts on aviation operations (Clark et al., 2000; Kim and Chun, 2010, 2011; Kim et al., 2019; Park et al., 2016, 2019), outdoor sport activities, and forest wildfires in a relatively drier environment under the fine weather conditions (Smith et al., 2018). Downslope windstorm can produce strong wind in the lee side and plays an essential role in creating and maintaining the wildfires near the northern California with the easterly winds across Sierra Nevada and the southern Cascade Mountains (Mass and Ovens, 2019). Lee et al. (2020) also suggested that the downslope windstorm favored the wildfires along the northeastern coast of Korea with the westerly winds across the Taebeak Mountain Range (TMR). The wind speed was also usually accelerated locally near the narrow valley or channel in between the mountains like the “gap wind” occurring along the strait of Juan de Fuca (Reed, 1931; Colle and Mass, 2000) in Washington, Columbia River Gorge in Oregon (Sharp, 2002), and Jangjeon area in South Korea (Lee et al., 2020).

Large-scale environmental conditions are key factors in determining the location where the downslope windstorm will be generated. The downslope windstorm usually occurs at the lee side, and the upstream prevailing wind direction is mostly perpendicular to the orientation of the mountain range. The elevated inversion-layer and the height of mean-state critical-level are also important references to evaluate the occurrence of downslope windstorm. The mechanisms of the downslope windstorm could usually be explained by hydraulic jump, partial reflection, and critical-level reflection from various numerical and theoretical studies in the past few decades

https://doi.org/10.5194/acp-2021-100
Preprint. Discussion started: 25 February 2021


Atmospheric Chemistry and Physics Discussions

(Long, 1953; Houghton and Kasahara, 1968; Klemp and Lilly, 1975; Smith, 1985; Durran, 1990; Afanasyev and Peltier, 1998; Epifanio and Qian, 2008; Rögnvaldsson et al., 2011; Cao and Fovell, 2016). The combination of hydraulic jump and wave breaking can also enhance the downslope windstorm and increase the wind speed (Shestakova et al., 2018; Tollinger et al., 2019). The pressure gradient force (PGF) is one of the possible factors that accelerate the wind speed near the exit of gap between the mountains (Reed, 1931; Finnigan et al., 1994; Colle and Mass, 2000).

A few previous studies provided insightful explanations in numerical aspect about the development of the strong wind associated with the downslope windstorm along the northeastern coast of South Korea (in the lee side of the Taebaek Mountain Ranges; TMR). Most strong downslope wind events can be mainly explained by the three mechanisms in this region: hydraulic jump, partial reflection, and critical-level reflection (Lee, 2003; Kim and Cheong, 2006; Jang and Chun, 2008; Lee and In, 2009). The strong wind possibly occurs in any season with appropriate environmental conditions such as westerly and upstream inversion. Lee et al. (2020) confirms these conclusions with numerical modeling studies. Furthermore, they also found that PGF is one of the possible factors to cause the gap wind, and the variability of PGF is highly related to the localized topographic features. However, it still lacks sufficient observational evidence to examine the strong downslope wind events in detail because relatively dense wind observations from ground-based remote sensing techniques could not be easily collected under fine weather conditions.

Pyeongchang hosted the Winter Olympic and Paralympic Games in 2018 (most venues are located at coastal and higher altitude areas of the TMR). More detailed weather conditions and accurate prediction for several key parameters such as precipitation, visibility, wind directions, and wind speed are very important to ensure the safety of all game players and attendees. The Numerical Modeling Center (NWC), Korea Meteorological Administration (KMA) organized an intensive field experiment named the International Collaborative Experiments for Pyeongchang

https://doi.org/10.5194/acp-2021-100
Preprint. Discussion started: 25 February 2021


Atmospheric Chemistry and Physics Discussions

2018 Olympic and Paralympic winter games, ICE-POP 2018 (http://155.230.157.230:8080/Icepop_2018/index.jsp). A very dense observational network was built to provide a good quality observational dataset in high temporal and spatial resolution either under precipitation or fine weather conditions. Many kinds of instruments were involved in the ICE-POP 2018 that allows the investigation of the nature of the strong wind event nearby mountainous areas in observational aspects.

Wider coverage of wind information can be usually obtained by the Doppler radar; however, regular meteorological Doppler radars cannot detect radial winds in fine weather conditions. Scanning Doppler lidar can be the best solution in obtaining a more complete wind information in such conditions even with finer resolutions. Using the Doppler lidar to document the downslope flow and rotors, Kühnlein et al. (2013) found that the transient internal hydraulic jump is characterized by turbulence. Menke et al. (2019) identified the recirculation zone over a complex terrain using six scanning Doppler lidars. The interactions between the winds and terrain essentially affected the occurrence of flow recirculation. However, only radial winds were used resulting in incomplete wind observations that can only provide very limited information for the realistic airflow structures. Complete 3D wind fields could be retrieved from 4DVAR (4D-Variational Assimilation) using Doppler lidar. The accuracy of wind speed, direction and water vapor flux will be improved when assimilating the lidar data (Kawabata, 2014). Thus, lidar observations can indeed provide a good quality of 3D wind information under fine weather condition.

The objective of this study is to use high spatiotemporal resolution of 3D winds and observational data to investigate the fine-scale structural evolution of strong downslope winds over the complex terrain in northeastern part of South Korea (i.e., in the Pyeongchang area) during the period 13–15 February 2018. Multiple Doppler lidars, automatic weather station (AWS), wind profiler, sounding observations, and local reanalysis (LDAPS: Local Data Assimilation and Prediction System) datasets were adopted to derive detailed 3D wind fields over

https://doi.org/10.5194/acp-2021-100
Preprint. Discussion started: 25 February 2021


Atmospheric Chemistry and Physics Discussions

136 TMR and northeastern coastal regions through the WISSDOM (WInd Synthesis System using
137 DOppler Measurements, Liou and Chang, 2009; Tsai et al., 2018) synthesis. In particular, this
138 study tries to recognize the mechanisms of the strong wind over the mountainous area and in the
139 lee side areas of TMR while a LPS passing through the northern side of the Korean peninsula. A
140 strong downslope wind case was selected for the further analysis in this study not only because
141 the Olympic games were interrupted due to the strong wind but also because dense observations
142 are available during the ICE-POP 2018. Interactions between the complex terrain and large-scale
143 airflow of the LPS could be adequately explored in this study. Furthermore, three scanning
144 Doppler lidars were established in this area, which provided more sufficient wind information
145 under fine weather condition.

146

147 **2 Data and methodology**

148 **2.1 Scanning Doppler lidar**

149 Two different models of scanning Doppler lidars were adopted in this study: (1) "WINDEX-
150 2000" produced by the manufacturer Laser Systems and (2) the "Stream Line" produced by the
151 manufacturer HALO Photonics. The scanning Doppler lidar can measure the radial Doppler
152 velocity by detecting atmospheric aerosols and dusts via laser (class 1M) in a very high spatial
153 resolution. The radial winds were sufficiently observed by adjustable scanning strategy in three
154 modes: Plan Position Indicator (PPI), Range Height Indicator (RHI), and Zenith pointing (ZP).
155 Furthermore, the complete wind information could be constructed using these lidar observations
156 under fine weather condition via WISSDOM.

157 The WINDEX-2000 lidar operated a full volume scan every ~27 min in which seven PPIs
158 (the elevation angles of 5º, 7º, 10º, 15º, 30º, 45º, and 80º) and one hemispheric RHI (the azimuth
159 angle of 0º, that is, started from the north). There are 344 gates along a radar radial direction with

https://doi.org/10.5194/acp-2021-100
Preprint. Discussion started: 25 February 2021


Atmospheric Chemistry and Physics Discussions

360 azimuth angles between 0º and 360º. The gate spacing is 40 m and the maximum observed radius distance is ~13 km. The Stream Line lidar operated a full volume scan every ~13 min in which five PPIs (7º, 15º, 30º, 45º, and 80º before 10:00 UTC on 14 Feb. 2018 and 4º, 8º, 14º, 25º, and 80º after 10:00 UTC) and two hemispheric RHIs (the azimuth angle of 51º and 330 º). There are 1660 gates along the 360 radar beams with azimuth angles between 0º and 360º. The gate spacing is 60 m and the maximum observed radius distance can reach to ~100 km.

Quality control (QC) of the radial winds (in PPI and RHI modes) was done by applying SNR (signal noise ratio) threshold in advance. To obtain correct and useful measurements, QC is necessary for each lidar observation, where the non-meteorological echoes are removed as the threshold of SNR is smaller than 0.04.

2.2 Surface weather station, sounding, wind profiler and LDAPS

Figure 1 shows an observational domain and domain of mountain clusters during the ICE-POP 2018. AWS mainly provides the surface wind speed, wind direction, pressure, and temperature in high spatiotemporal resolution (1-min interval and ~10 km distance between each AWS station). In addition to the regular KMA AWS, additional AWS sites were deployed in the mountainous area during the ICE-POP 2018. Thus, dense AWS network (black dots in Fig. 1b) can be utilized to document detailed evolutions of surface parameters and could also be observational inputs for WISSDOM (the details is Section 2.3). Five soundings are launched every 3 hours and the sounding sites are all located in the studied domain near the northeastern part of South Korea (black square in Fig. 1a). Such dense sounding observations provide environmental winds, temperature profiles, and stability information in a very fine-scale across the mountainous and coastal areas. The wind profiler is deployed at the GWW site to measure the winds in case of lacking sounding observations. In addition, the high temporal resolution of wind profiler measurements (10-min interval) could potentially be reference for the surface and

https://doi.org/10.5194/acp-2021-100
Preprint. Discussion started: 25 February 2021

Atmospheric Chemistry and Physics Discussions

retrieved winds.

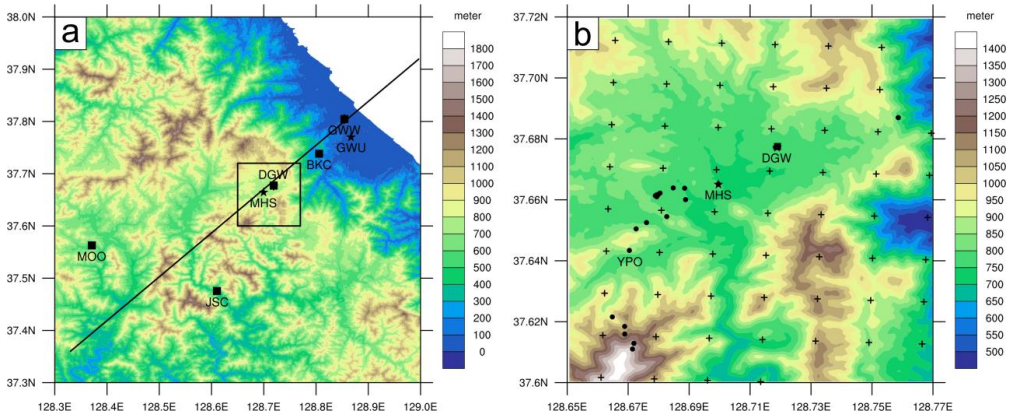

Figure 1. (a) Observations used in this study and the topographic features from the DEM (digital elevation model) in the northeastern Korea (corresponding to the bigger box in the Fig. 3) and (b) WISSDOM synthesis domain adopted in this study corresponding to the box in Fig. 1a. The locations of the scanning Doppler lidar sites are denoted by asterisks. The locations of the sounding sites are denoted by squares. Note that the sounding and lidar observations are both operated at DGW site and a wind profiler is located at GWW site. The locations of the AWS sites and LDAPS grids are denoted by dots and plus symbols, respectively.

The LDAPS is a 3DVAR numerical weather prediction (NWP) product generated from KMA with a spatial (temporal) resolution of ~1.5 km (3 hours) with 70 levels in vertical. High resolution 3D wind fields from LDAPS will be one of the "observational" inputs in WISSDOM. This dataset is freely available from the KMA web site (https://data.kma.go.kr). Note that a relatively weaker weighting of the LDAPS input will be set in WISSDOM because this study prefers to emphasize the contribution from the observations.

2.3 WInd Synthesis System using DOppler Measurements (WISSDOM)

WISSDOM was originally developed by Liou and Chang (2009) and has been applied in the Pyeongchang area (Tsai et al., 2018). This study adopted a newly improved version, which includes more observations with more constraints compared with a previous version. In new version of WISSDOM, the following cost function [eq. (1)] was minimized by using

https://doi.org/10.5194/acp-2021-100
Preprint. Discussion started: 25 February 2021


Atmospheric Chemistry and Physics Discussions

mathematical variational-based method at the retrieval time,

$$J = \sum_{M=1}^{8} J_M . \tag{1}$$

This cost function comprised of eight constraints, and the 3D wind fields were obtained by variationally adjusting solutions to simultaneously satisfy those constraints at the same time. The first constraint is the geometric relation between the radial velocity (V_r) observations from multiple lidars and Cartesian winds $V_t = (u_t, v_t, w_t)$, control variables, defined as

$$J_1 = \sum_{t=1}^{2} \sum_{x,y,z} \sum_{i=1}^{N} \alpha_{1,i} \left(T_{1,i,t}\right)^2, \tag{2a}$$

$$T_{1,i,t} = (V_r)_{i,t} - \frac{\left(x - P_x^i\right)}{r_i} u_t - \frac{\left(y - P_y^i\right)}{r_i} v_t - \frac{\left(z - P_z^i\right)}{r_i} \left(w_t - W_{T,t}\right), \text{and} \tag{2b}$$

$$r_i = \sqrt{\left(x - P_x^i\right)^2 + \left(y - P_y^i\right)^2 + (z - P_z^i)^2}. \tag{2c}$$

Any numbers of lidar [subscripts i in eq. (2a)] can be applied to this constraint at two time levels (subscripts t). α_1 in eq. (2a) is the weighting coefficient corresponding to J_1 (same as the following equations for J_2 - J_8). The subscripts i and t in the $(V_r)_{i,t}$ represent the radial velocity observed by the i-th lidar, and (u_t, v_t, w_t) indicate the 3D wind at location (x, y, z), and the terminal velocity ($W_{T,t}$) of particles were estimated by radar reflectivity at two time levels. $\left(P_x^i, P_y^i, P_z^i\right)$ are the coordinates of the i-th lidar, and the distance between each grid point and the i-th lidar were denoted by r_i. Note that $W_{T,t}$ will be zero when there is no radar reflectivity, or the terminal velocity is possibly negligible under fine weather condition.

Next constraint is the difference between the $\mathbf{V}_t$ and the background winds ($\mathbf{V}_{B,t}$) defined in eq. (3);

$$J_2 = \sum_{t=1}^{2} \sum_{x,y,z} \alpha_2 \left(\mathbf{V}_t - \mathbf{V}_{B,t}\right)^2, \tag{3}$$

the sounding observations are used to be the background winds in eq. (3). The constraint of the anelastic continuity equation is

https://doi.org/10.5194/acp-2021-100
Preprint. Discussion started: 25 February 2021

Atmospheric Chemistry and Physics Discussions

$$J_3 = \sum_{t=1}^{2} \sum_{x,y,z} \alpha_3 \left[\frac{\partial(\rho_0 u_t)}{\partial x} + \frac{\partial(\rho_0 v_t)}{\partial y} + \frac{\partial(\rho_0 w_t)}{\partial z} \right]^2, \quad (4)$$

where ρ_0 is the air density. The fourth constraint was deduced from the vertical vorticity equation given by

$$J_4 = \sum_{x,y,z} \alpha_4 \left\{ \frac{\partial \xi}{\partial t} + \left[u\frac{\partial \xi}{\partial x} + v\frac{\partial \xi}{\partial y} + w\frac{\partial \xi}{\partial z} + (\xi + f)\left(\frac{\partial u}{\partial x} + \frac{\partial v}{\partial y}\right) + \left(\frac{\partial w}{\partial x}\frac{\partial v}{\partial y} - \frac{\partial w}{\partial y}\frac{\partial u}{\partial z}\right) \right] \right\}^2, \quad (5)$$

where f indicate the Coriolis parameter and the meaning of overbar in eq. (5) is the temporal average of the two time levels. The constraint about Laplacian smoothing filter:

$$J_5 = \sum_{t=1}^{2} \sum_{x,y,z} \alpha_5 [\nabla^2 (u_t + v_t + w_t)]^2. \quad (6)$$

The horizontal winds observed by the sounding, AWS and LDAPS, can be interpolated to each given grid in the WISSDOM synthesis domain. The sixth constraint is the difference between the $\mathbf{V}_t$ and the sounding observations ($\mathbf{V}_{S,t}$), as defined in eq. (7);

$$J_6 = \sum_{t=1}^{2} \sum_{x,y,z} \alpha_6 (V_t - V_{S,t})^2. \quad (7)$$

The seventh constraint represents the discrepancy between the surface winds and AWS ($\mathbf{V}_{A,t}$), as expressed in eq. (8);

$$J_7 = \sum_{t=1}^{2} \sum_{x,y,z} \alpha_7 \left(V_t - V_{A,t}\right)^2. \quad (8)$$

Finally, the eighth constraint measures the squared errors between the horizontal winds and the LDAPS ($\mathbf{V}_{L,t}$), as defined in eq. (9);

$$J_8 = \sum_{t=1}^{2} \sum_{x,y,z} \alpha_8 (V_t - V_{L,t})^2. \quad (9)$$

Original version of WISSDOM is just only included first five constraints, it had already applied to synthesize high-quality 3D wind field in some of previous studies (Liou and Chang, 2009;

https://doi.org/10.5194/acp-2021-100
Preprint. Discussion started: 25 February 2021


Atmospheric Chemistry and Physics Discussions

Liou et al., 2012, 2013, 2014, 2016; Lee et al., 2017). The primary advantages and additional details of WISSDOM can be referred to Tsai et al. (2018). The main improvement of the new version of WISSDOM is that all available wind observations are considered to be one of the constraints to minimize the cost function. In addition, this new version extends its applicability by including multiple-lidar observations and thus, realistic wind fields would be retrieved under fine weather condition.

3 Overview of the strong wind case

3.1 Synoptic condition

Hourly ERA5 dataset was used herein to document the synoptic condition. The ERA5 data is an atmospheric reanalysis of the globe climate and was generated by the European Centre for Medium-Range Weather Forecasts (ECMWF, DOI: 10.24381/cds.adbb2d47). In the beginning of the research period at 12:00 UTC on 13 February 2018, a high-pressure system (HPS) was located in the southernmost of the Korean peninsula (as Fig. 2a). Surface southwesterly winds were dominant from the Yellow sea to the western coast of South Korea associated with anti-cyclonic circulation of the HPS. This stronger southwesterly wind was also related to the cyclonic circulation of a low-pressure system (LPS) centered at 39^{o}N, 117^{o}E near Beijing, China. Compared to the western coast, relatively weak wind existed over the land and eastern coast of Korea. The westerly wind came from China accompanying warm air at a higher layer (850 hPa, Fig. 2b). This veering wind also indicated that the prevailing southwesterly wind was dominated by the warm advection. Thus, the temperature gradient existed between the land, western and eastern coast (exceeding ~4^{o}K difference).

https://doi.org/10.5194/acp-2021-100
Preprint. Discussion started: 25 February 2021

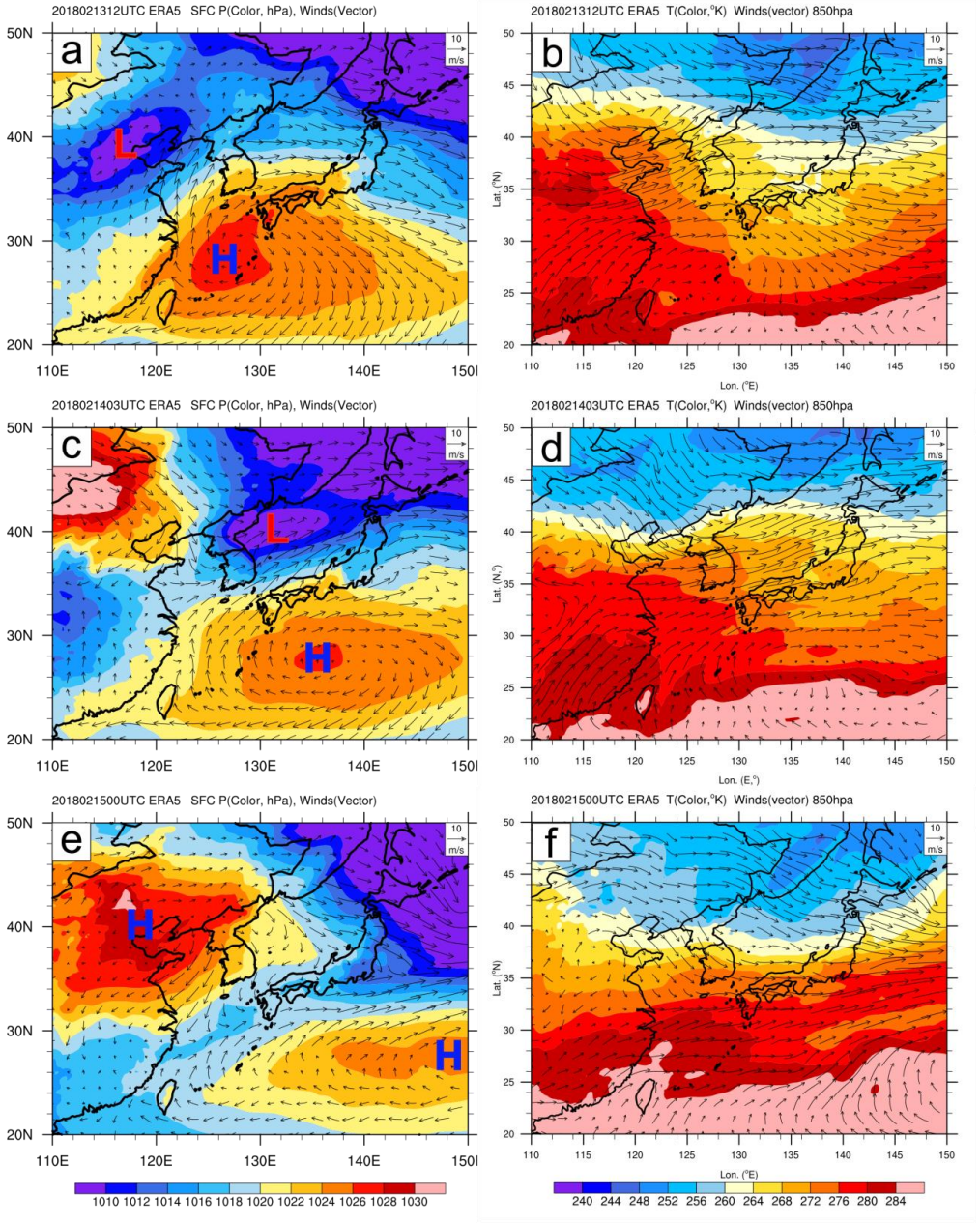

Figure 2. (Left panels) Horizontal winds (vectors) and surface pressure (hPa, color shading) at the surface level obtained from the ERA5 reanalysis dataset at (a) 12:00 UTC on 13 Feb., (c) 03:00 UTC on 14 Feb. and (e) 00:00 UTC on 15 Feb. 2018. (Right panels) Horizontal winds (vectors) and temperature (°K, color shading) at 850 hPa level from the same reanalysis at (b) 12:00 UTC on 13 Feb., (d) 03:00 UTC on 14 Feb. and (f) 00:00 UTC on 15 Feb. 2018. The locations of low (high) pressure systems are marked by "L" ("H").

https://doi.org/10.5194/acp-2021-100
Preprint. Discussion started: 25 February 2021


Atmospheric Chemistry and Physics Discussions

271 Consequently, the LPS and HPS were both moving eastward. The surface wind became
272 stronger and turned to westerly over the Korean peninsula associated with the confluences
273 between these two systems (Fig. 2c). Horizontal pressure gradient was intensified along the
274 northeastern coast of Korea as the LPS moved to the East Sea. A relatively lower temperature
275 was detected over the mountain area (i.e., near northeastern coast of South Korea) even when the
276 warm advection was approaching Korea (Fig. 2d**)**. The other HPS came from China at around
277 00:00 UTC on 15 February 2018 and the environmental winds surrounding Korea were switched
278 to relatively weak northerly winds. Relatively weaker pressure gradient and smaller temperature
279 differences between the western and eastern coasts were shown in Figs. 2e and 2f. No
280 precipitation existed along the northeastern coast of South Korea according to the AWS
281 observations during the research period (not show).
282 The research period can be separated into two stages based on the synoptic conditions as the
283 LPS was approaching (between 18:00 UTC on 13 February and 09:00 UTC on 14 February 2018)
284 and leaving (09:00 UTC on 14 February and 00:00 UTC on 15 February 2018) from Korea.
285 Spatial distribution of linear trends (percentage h^{-1}, Chou et al., 2013) of surface wind speed for
286 these two stages were shown in Fig. 3. Generally, the surface wind speed was increased by ~2–8
287 percentage h^{-1} while the LPS was approaching Korea and higher increasing trend (over than 10
288 percentage h^{-1}) was related to the upstream of mountain ranges and the east coast (lee side of the
289 TMR) in Korea (Fig. 3a). In addition, the strong positive spatial gradient appeared from the TMR
290 to the east coast along with negative trends over the mountain ranges as described in the Fig. 3a.
291 That is, the surface wind speed slightly decreased or nearly constant (~10 m s^{-1}) over the TMR
292 while the LPS was approaching. The surface wind speed dramatically increased with the
293 approaching LPS. When the LPS was moving away from the east coast, the negative trend is
294 dramatic, in particular, over the TMR and east coastal regions (Fig. 3b).

https://doi.org/10.5194/acp-2021-100
Preprint. Discussion started: 25 February 2021

Atmospheric Chemistry and Physics Discussions

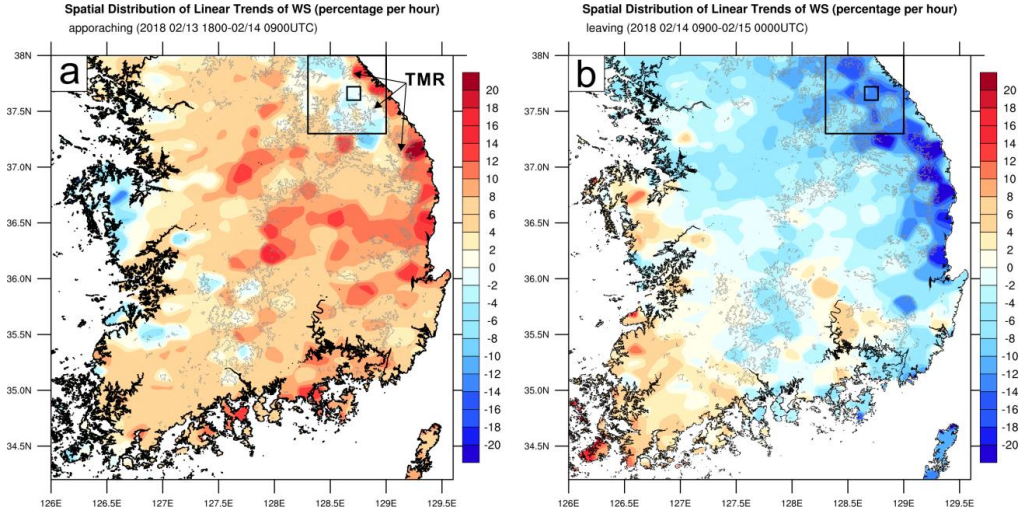

Figure 3. (a) Spatial distribution of linear trends of surface wind speed (unit: percentage h^{-1}, color shading) calculated from the AWS (automatic weather station) observations during the low-pressure system (LPS) approaching from 18:00 UTC on 13 to 09:00 UTC on 14 Feb. 2018. (b) as in (a) but for the time period when the LPS was leaving from 09:00 UTC on 14 to 00:00 UTC on 15 Feb. 2018. The topographic height thresholds of 600 m MSL (mean sea level)is indicated by gray lines and the arrows marked the location of the TMR.

3.2. Environmental conditions in the local area near northeastern Korea

Because the spatial distribution of linear trends of surface wind speed revealed obvious gradient just near the mountainous area and in the lee side of the TMR, two domains were selected in this study that are shown as boxes in Fig. 3. All available intensive observations are also marked in Figs. 1a and 1b, corresponding to the bigger and smaller boxes in Fig. 3. Three scanning Doppler lidars were deployed at DGW, GWU (Stream Line), and MHS (WINDEX-2000), indicated by asterisks in Fig. 1a. Five sounding stations aligned from the mountainous area to the coastal area (i.e., perpendicular with the orientation of TMR). The sounding stations MOD and JSC were located at the southwestern TMR with gentle slope and the station DGW was the closest site to most outdoor venues of the Olympic games near the crest of TMR. Station BKC and GWW were located at the northeastern slope of TMR and the coast area, respectively (as Fig. 1a). In addition, a wind profiler is located at the lee side (GWW). The WISSDOM

https://doi.org/10.5194/acp-2021-100
Preprint. Discussion started: 25 February 2021


Atmospheric Chemistry and Physics Discussions

313 synthesis domain was set over the mountainous area with a horizontal spatial coverage of 12 ×
314 12 km^2 as shown in Fig. 1b. The horizontal and vertical grid size were both set to 50 m, and
315 vertical extension is from 0- km to 3- km height MSL (mean sea level). Additional AWS stations
316 were deployed around the venues (black dots in Fig. 1b) during the ICE-POP 2018. Furthermore,
317 the location of the LDAPS reanalysis dataset was also marked by the plus symbols.

318 Figure. 4 shows the variations in the environmental winds observed by the soundings and/or
319 wind profiler along the crossline (black line in Fig. 1a) from the mountainous area to the lee side.
320 Instead of lacking sounding observations at GWW site, the wind profiler observation is used to
321 provide the wind information near the coastal area when the LPS was passing Korea. In the
322 beginning of the research period, prevailing westerly winds are dominant at all sounding sites
323 (Fig. 4a). However, a relatively stronger wind was only measured in heights below ~1.5 km 184
324 at the DGW site near the crest of the TMR (~25 m s^{-1}), and weaker wind (<15 m s^{-1}) were
325 observed at other sites (MOO, BKC, and GWW) in lower layers on both windward slope and lee
326 side. The wind direction still revealed westerly at 03:00 UTC on 14 February 2018 (as Fig. 4b).
327 However, strong winds were detected at the TMR (DGW) and in the downslope with a wind
328 speed larger than 20 m s^{-1} above the BKC and GWW sites. Although the wind speed becomes
329 stronger above 1.5 km MSL over the DGW site, it did not exhibit a significant change near the
330 surface. The results demonstrated that persistent strong winds existed over the mountainous area
331 (i.e., near the DGW site) while the LPS was approaching. After the LPS passed Korea, all
332 sounding sites exhibited the wind speed weakened near the surface (Fig. 4c).

https://doi.org/10.5194/acp-2021-100
Preprint. Discussion started: 25 February 2021

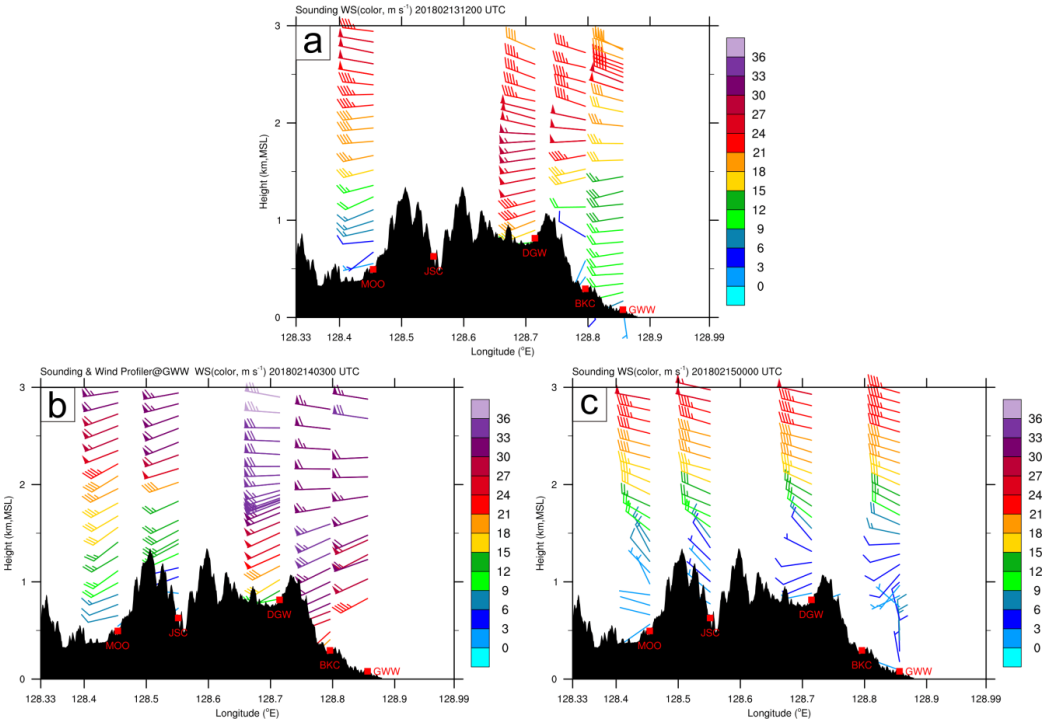

Figure 4. Horizontal winds observed by sounding and wind profiler along the cross line corresponding to Fig. 1a at (a) 12:00 UTC on 13 Feb. 2018, (b) 03:00 UTC on 14 Feb., and (c) 00:00 UTC on 15 Feb. 2018. A full wind barb corresponds to 5 m s^{-1}; a half barb corresponds to 2.5 m s^{-1}. The color indicates the wind speed correspond to bars. The black shading in the lower portion indicates the averaged topography along the line in Fig. 1a.

Detailed environmental conditions in the upstream of the lee site (or the TMR area) was investigated by the sounding observations at the DGW site (Fig. 5). An inversion layer existed around 800 hPa height mainly due to the warm advection accompanied by the southwesterly at 850 hPa ahead of the LPS (Figs. 2a and 2b at 12:00 UTC on 13 Feb. 2018) until it was passing through the Korea peninsula (at 03:00 UTC on 14 Feb. 2018). The temperature was increasing near the surface and became drier above the inversion layer between the two time steps. The wind direction comprised of westerly at all levels while the LPS was passing through. The wind speed became stronger above the inversion layer, but it exhibited no clear changes below ~800 hPa. It is worth to mention that the inversion layer was mainly developed by two contributions: (1) large-scale warm advection and (2) stable boundary layer. Their separate contributions would require

https://doi.org/10.5194/acp-2021-100
Preprint. Discussion started: 25 February 2021

Atmospheric Chemistry and Physics Discussions

348 a modeling study for this case in the future. The sounding observations showed a good condition
349 for generating hydraulic jump and downslope windstorm in the lee side (Lee et al. 2020).
350 In summary, the environmental winds were mostly westerly in this case. However, the wind
351 speeds revealed different characteristics at mountainous area and lee side. Strong winds (~10 m
352 s^{-1}) persist near the surface on the mountainous area and the wind speed dramatically increased
353 in the lee side.

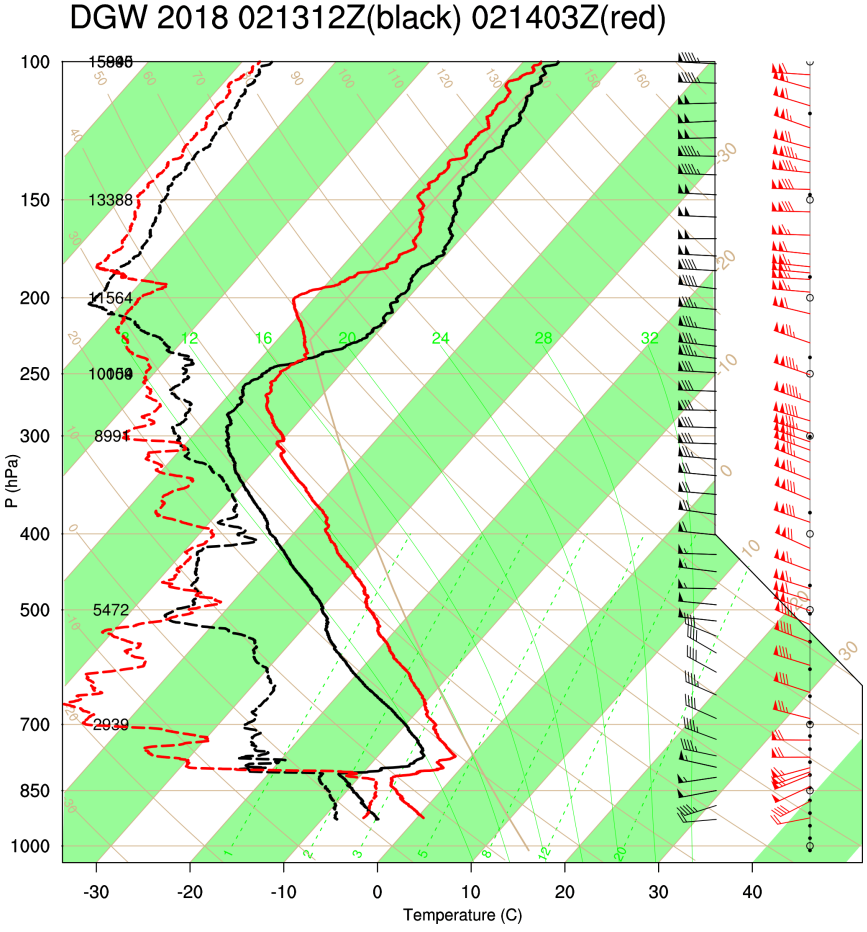

354
355 **Figure 5.** Profiles of temperature (solid lines), dew point (dashed lines), and horizontal winds observed by sounding
356 at the DGW site at 12:00 UTC on 13 Feb. (black lines) and 03:00 UTC on 14 Feb. (red lines) 2018. A full wind barb
357 corresponds to 5 m s^{-1} and a half barb corresponds to 2.5 m s^{-1}.

https://doi.org/10.5194/acp-2021-100
Preprint. Discussion started: 25 February 2021


Atmospheric Chemistry and Physics Discussions

4 Stronger winds in the lee side

4.1 The lidar and AWS observations

Although the environmental wind direction likely westerly, the wind speed had a dramatic increasing trend in the lee side of the TMR. The detailed wind speed and surface fluctuations were documented by lidar quasi-vertical profile (QVP, Ryzhkov et al., 2016) at GWU site (upper panel) and the AWS observations at GWW site (lower panel) as shown in Fig. 6. The wind speed was relatively weak around 6- 9 m s^{-1} at the lowest layer in the beginning of the research period. Strong winds were then measured by the lidar QVP reaching ~36 m s^{-1} up to ~1.5 km MSL after 00:00 UTC on 14 February 2018 (as Fig. 6a). It was clear that strong upper winds propagate toward the lower layer, intensify the wind speed near surface between 03:00 UTC and 09:00 UTC. Finally, the wind speed became weak after 09:00 UTC on 14 February. Winds observed from the sounding and wind profiler were consistent with these QVP winds (cf. Fig. 4).

Fluctuations in wind speed, direction, perturbation pressure and perturbation temperature at GWW site were shown in Fig. 6b. The changes of wind speed were similar to the lowest layer of lidar observations (cf. Fig. 6a). Relatively weak winds were measured at the early stage of the period and the surface wind speed was intensified dramatically exceeding ~12 m s^{-1} between 00:00 and 06:00 UTC on 14 February (named as speed-up stage and highlighted by shaded area in the Fig. 6). The surface wind direction also showed similar patterns to the lidar observations as it had minor changes from more southerly to westerly. Although these two stations were at different locations along the northeastern coast of Korea, they revealed consistent changes on wind fields. The results also implied that the wind fields along the coast and in the lee side of the TMR have almost the same characteristics, which could be verified by the linear trend distribution of the surface wind speed (cf. Fig. 3a). Negative perturbation temperature was measured within the first 12 hours in the beginning of the period and increased after 00:00 UTC on 14 February

https://doi.org/10.5194/acp-2021-100
Preprint. Discussion started: 25 February 2021

Atmospheric Chemistry and Physics Discussions

382 from ~ −3 ºC to 4 ºC. The fluctuation of perturbation pressure showed an opposite phase with the
383 perturbation temperature with the changing magnitude from around 5 to −6 hPa. The wind speed
384 was increasing just after the perturbation temperature (pressure) was rising (dropping). That is, a
385 significant lag between T' (P') and wind speed is evident. Their specific relationships and
386 mechanisms will be clarified through a more detailed analysis in Section 4.2.

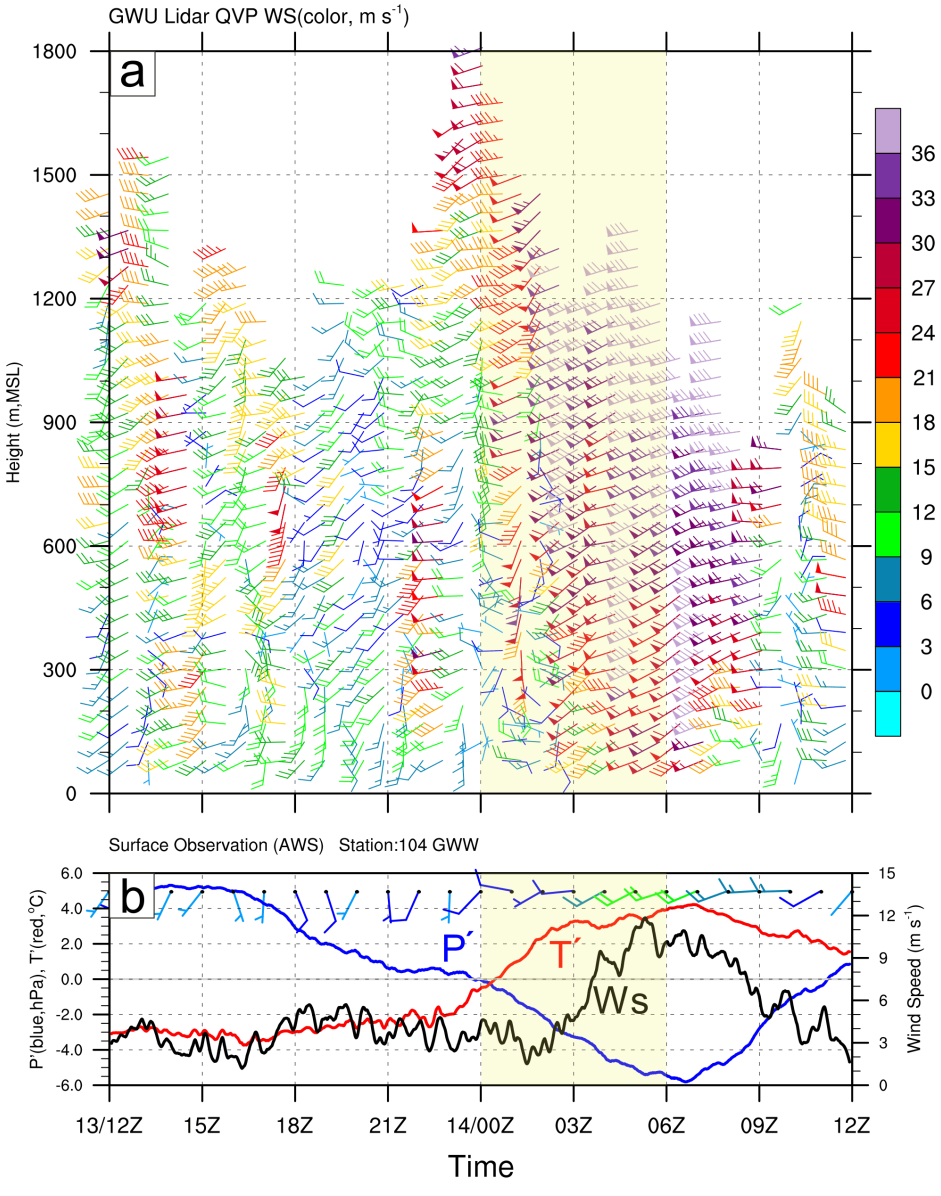

387

https://doi.org/10.5194/acp-2021-100
Preprint. Discussion started: 25 February 2021


Atmospheric Chemistry and Physics Discussions

388 **Figure 6.** (a) Time series of QVP (quasi-vertical profile) from lidar observations at GWU site during 12:00 UTC on
389 13 Feb. to 12:00 UTC on 14 Feb. 2018. A full wind barb corresponds to 5 m s^{-1}; a half barb corresponds to 2.5 m
390 s^{-1} and the color indicates the wind speed (m s^{-1}) correspond to color scale. (b) Time series of horizontal winds (wind
391 barbs), wind speed (m s^{-1}, black line), perturbation pressure (hPa, P', blue line) and perturbation temperature (ºC, T',
392 red line) observed from the AWS at GWW site. The time period with accelerating wind speed is also highlighted by
393 light yellow shading (i.e., speed-up stage).

394 **4.2 Possible mechanism of strong winds in the lee side**

395 The winds can usually be accelerated by the PGF between the two sites as the stronger wind
396 usually occurred at the site where lower pressure was located. Therefore, the DGW site was
397 selected as the upstream from the GWW site, and the differences between the surface temperature
398 and sea level pressure will be analyzed. A relatively warm environment was presented in the lee
399 side of the TMR and the temperature between the DGW and GWW sites suddenly increases from
400 ~7 ºC in the beginning of the research period to ~8.5 ºC after 00:00 UTC on 14 February (Fig.
401 7a). The expected temperature difference between the two sites is about 6.9 ºC (adiabatic cooling
402 rate for 0.7 km height difference) when the adiabatic heating assumed. The sea level pressure
403 also decreased from ~−1 hPa to −4 hPa at the time when the temperature was raising. The
404 observed wind speed at the GWW site showed no obvious changes in the beginning. However,
405 the wind speed has significantly increased just ~1 hour after the sea level pressure (temperature)
406 was decreasing (raising). This result revealed that the changes of wind speed are possibly related
407 to the fluctuation of temperature and pressure. To clarify the role of pressure gradient on the wind
408 speed at the DGW site, the local accelerations between the two sites could be approximated based
409 on the horizontal momentum equation expressed as

410 $$\underbrace{\frac{\partial u}{\partial t}}_{A} = \underbrace{-u\frac{\partial u}{\partial x}}_{B} \underbrace{-\frac{1}{\rho}\frac{\partial P}{\partial x}}_{C} + \underbrace{fv}_{D} + \underbrace{\frac{C_d W_s u}{H}}_{E}. \quad (10)$$

411 In equation (10), Term A is the changes of u component with the time, which also
412 corresponds to the wind accelerations along the west-east direction and Term B is the advective

https://doi.org/10.5194/acp-2021-100
Preprint. Discussion started: 25 February 2021


Atmospheric Chemistry and Physics Discussions

413 acceleration amount to the distance (x) between these two selected sites. Only the u component
414 was considered in this study since the v and w components could be neglected because the
415 environmental winds mostly comprised of westerlies (Yu et al., 2020). The PGF was indicated
416 by Term C, where the ρ is air density and the P is sea level pressure. Coriolis acceleration and
417 friction were indicated by Term D and Term E, respectively, where the C_d, W_s, and H in Term
418 E are the drag coefficient, wind speed and boundary layer height. The value of drag coefficient
419 would most likely be a unitless constant based on Stull (1988) and was set as ~3.9×10^{-3} in this
420 study. The height of H used in this study was ~150 (1500) m MSL according to the GWW
421 (DGW) sounding observations at 00:00 UTC on 14 February 2018 (not shown).

422 Basically, the wind acceleration (i.e., Term A) that is derived from the equation (10) by
423 adding terms from B to E is in good agreement with the fluctuation of wind speed at GWW site
424 (Fig. 7b). A relatively weak wind speed occurred in the beginning and is coincident with negative
425 and weak accelerations. Consequently, the wind speed jumped at GWW site in the speed-up stage
426 (i.e., shading area in Fig. 7) associated with the increased and positive accelerations (i.e., Term
427 A). Furthermore, the contribution of Terms B~E into Term A could also be evaluated individually
428 by calculating each Term. PGF (Term C) dominated the changes of Term A with almost the same
429 magnitudes during the entire research period as shown in Fig. 7c. In the beginning, the advective
430 acceleration (Term B) can provide a little bit of positive contribution to Term A while PGF term
431 is negative. However, both Term B and friction (Term E) gave negative feedback to Term A in
432 the speed-up stage. Coriolis acceleration (Term D) always exhibited an almost zero acceleration
433 to Term A due to sub-synoptic scale feature. The results suggested that the PGF would be the
434 main factor to dominate the changes of wind speed at the GWW site in the lee side.

https://doi.org/10.5194/acp-2021-100
Preprint. Discussion started: 25 February 2021

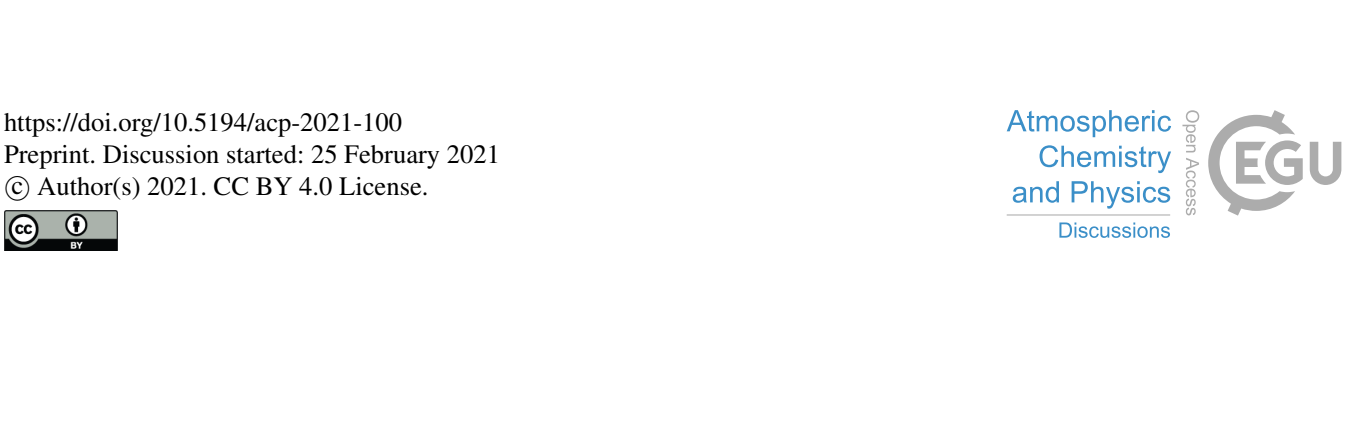

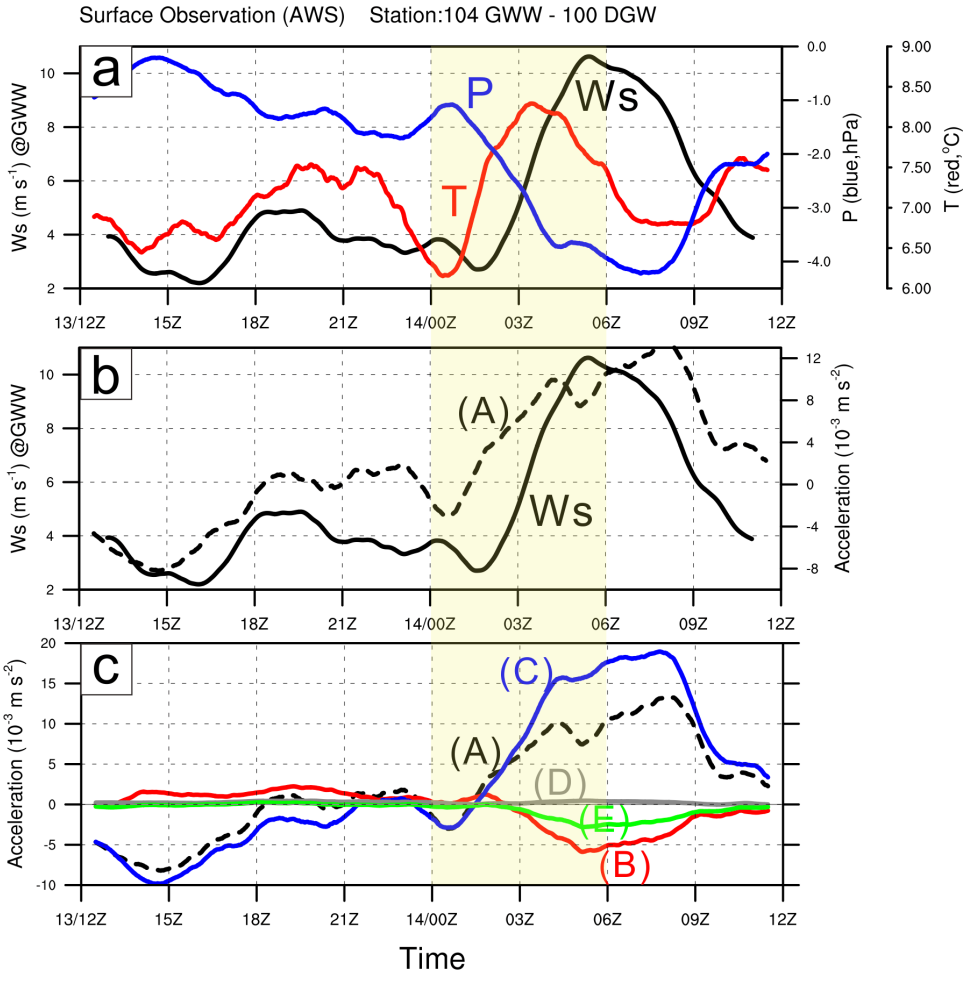

Figure 7. (a) Time series of wind speed (m s^{-1}, black line) observed from the AWS at GWW site, and the differences of sea level pressure (hPa, blue line), temperature (°C, red line) between the GWW and DGW sites from 12:00 UTC on 13 Feb. to 12:00 UTC on 14 Feb. 2018. (b) Time series of the u component acceleration (10^{-3} m s^{-2}, Term A, black dashed line) estimated from the horizontal momentum equation [eq. (10)] between GWW and DGW sites. (c) Time series of the u component acceleration (Term A, black dashed line), the advective acceleration (Term B, red line), the PGF (Term C, blue line), Coriolis acceleration (Term D, gray line), and friction (Term E, green line). The time period with accelerating wind speed is also highlighted by light yellow shading (i.e., speed-up stage).

Since the gusty wind can be explained by PGF, this result is also consistent with the fluctuations in the perturbation pressure from the AWS observations at GWW site (cf. Fig. 6b) as the observed perturbation pressure always comprised of negative values with the maximum of ~ -6 hPa during the speed-up stage. To understand the possible causes of the relatively lower

https://doi.org/10.5194/acp-2021-100
Preprint. Discussion started: 25 February 2021


Atmospheric Chemistry and Physics Discussions

447 pressure occurring in the lee side area, more detailed analysis is needed. The surface perturbation
448 pressure can be estimated by solving the integration of the vertical momentum equation (Yu and
449 Tsai, 2010),

450 $$P_S' = \underbrace{\int_0^{Z_T} \rho_0 \left(\frac{\partial w}{\partial t} + u\frac{\partial w}{\partial x} + v\frac{\partial w}{\partial y} + w\frac{\partial w}{\partial z}\right)}_{A} + \underbrace{\int_0^{Z_{LCL}} -\rho_0 g \frac{T_v'}{T_{v0}} dZ}_{B}$$

451 $$+ \underbrace{\int_{Z_{LCL}}^{Z_T} -\rho_0 g \frac{T_v'}{T_{v0}} dZ}_{C} + \underbrace{\int_0^{Z_T} \rho_0 g q_r dZ}_{D}, \quad (11)$$

452 where P_S' is surface perturbation pressure, ρ_0 is the reference air density function of height, and
453 T_{v0} and T_v' are the reference and perturbation virtual temperature obtained from surface
454 observations. The g and q_r in equation (11) correspond to the gravity acceleration and
455 rainwater mixing ratio, respectively. Z_{LCL} and Z_T indicate the height of the lifting condensation
456 level (LCL) and the cloud top, respectively. The LCL (~1900 m) can be calculated from the
457 averaged sounding observations at GWW during the period. The terms on the right-hand side in
458 equation (11) are different contributions to the estimated surface pressure (P_S') including
459 nonhydrostatic effect (Term A), sub-cloud and in-cloud warming/cooling (Terms B and C), and
460 water loading (Term D).

461 The Terms C and D would be possibly neglected since the studied case just occurred under
462 fine weather condition. Remaining contributions for the estimated perturbation pressure may
463 come from the nonhydrostatic effect (Term A) and in-cloud warming/cooling (Term B) because
464 this study ignored the in-cloud warming/cooling and water loading. The estimated values of Term
465 B have ~1 (~2) hPa underestimated (overestimated) from the observed perturbations pressure at
466 ~15:00 (21:00) UTC on 13 February in advance of the speed-up stage and there is about 2 hPa ~
467 3 hPa difference after 09:00 UTC on 14 February. Nevertheless, the estimated values of Term B
468 are in good agreement with the observed perturbations pressure without significant differences
469 (Fig. 8) in speed-up stage. The results suggested that the origin of the lower pressure in the lee
470 side of TMR was deduced by sub-cloud warming. Such PGF could accelerate the wind speed in

https://doi.org/10.5194/acp-2021-100
Preprint. Discussion started: 25 February 2021

Atmospheric Chemistry and Physics Discussions

the speed-up stage in the lee side of the mountains.

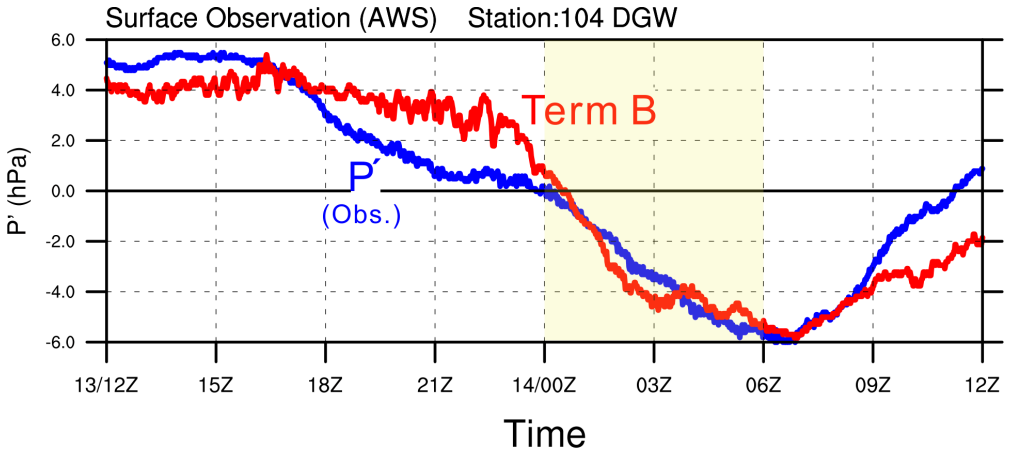

Figure 8. Time series of perturbation pressure (unit: hPa) observed by the AWS (blue line) and estimated Term B (sub-cloud cooling/warming, red line) in the vertical momentum equation [eq. (11)] at the GWW site from 12:00 UTC on 13 Feb. to 12:00 UTC on 14 Feb. 2018. The time period with accelerating wind speed is also highlighted by light yellow shading (i.e., speed-up stage).

4.3 Mountain wave, hydraulic jump, and downslope windstorm

The mountain wave feature was detected in the local reanalysis data of the LDAPS (Fig. 9). Alternative downdraft and updraft were presented near the crest (near DGW site) and the lee side of the TMR at 21:00 UTC on 13 February 2018 (at 3 hours prior to the speed-up stage, Fig. 9a). The mountain wave propagated toward the northeastern direction (parallel to The TMR) associated with the interactions between the prevailing west-southwesterly winds and topography (lee wave in Fig. 9a). Stronger downdraft and updraft were characterized by positive and negative phases stronger than 3 m s^{-1} at DGW, BKC and GWW sites and the phase lines were parallel with the orientation of the TMR. Subsequently, in the speed-up stage, the mountain wave structures significantly changed at 03:00 UTC on 14 February 2018. The wavelength became longer but the wave still parallel to the TMR and the northeastern coast (Fig. 9b).

https://doi.org/10.5194/acp-2021-100
Preprint. Discussion started: 25 February 2021

Atmospheric Chemistry and Physics Discussions

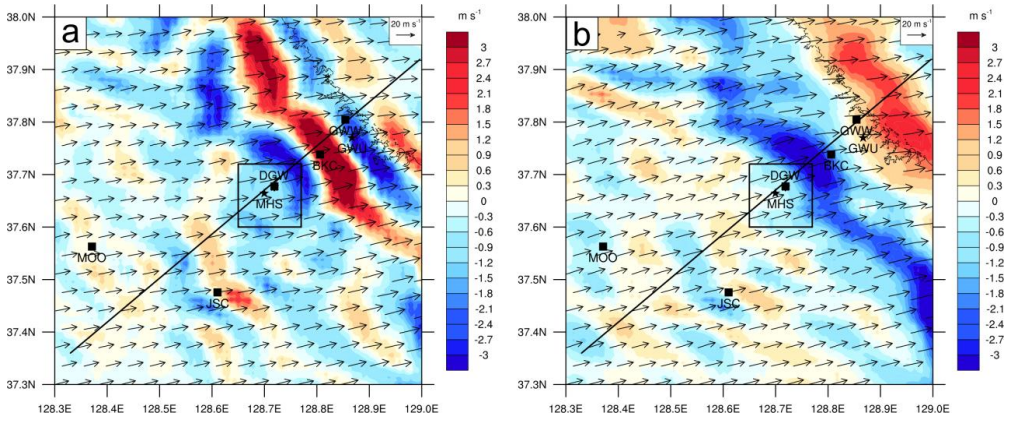

488

489 **Figure 9.** Horizontal distribution of the vertical velocity (m s^{-1}, color shading) and horizontal winds (vectors) at 2
490 km MSL from the LDAPS in the domain corresponding to the Fig. 1a at (a) 21:00 UTC on 13 Feb. 2018 and (b)
491 03:00 UTC on 14 Feb. 2018. The locations of the scanning Doppler lidars (soundings) sites are denoted by asterisks
492 (squares).

493 The cross section of the potential temperature (thick solid line in Fig. 10) and streamwise
494 velocity (colors in Fig. 10) perpendicular with the orientation of the TMR demonstrated the
495 mountain wave characteristics in the lee side (between the DGW and GWW sites) at 21:00 UTC
496 on 13 February 2018 (Fig. 10a). In this time period, a relatively stronger streamwise velocity only
497 occurred near the downslope of the TMR (~128.78ºE, ~1 km MSL) and coincides with the
498 stronger downdraft. Weaker streamwise velocity (<4 m s^{-1}) appeared near the GWW site in the
499 coastal area. However, the potential temperature pattern in the speed-up stage was characterized
500 by a longer wavelength with higher amplitude of the mountain wave (Fig. 10b), which is
501 consistent with the vertical velocity field (Fig. 9b). A stronger wind exceeding 30 m s^{-1} (shaded
502 orange colors in Fig. 10b) stemmed from higher altitudes as jet stream was approaching the
503 Korean peninsula at this time. The strong wind propagated down to 0.5 km toward the GWW
504 site. Note that the maximum values of Froude number related to the environmental winds at the
505 DGW sounding site were estimated around 0.55–0.89. These Froude number were calculated
506 from the sensitivity test using dry and saturated Brunt-Vaisala frequency and increasing the
507 topographic height between 1000 and 2000 MSL. These structures were similar to the hydraulic

https://doi.org/10.5194/acp-2021-100
Preprint. Discussion started: 25 February 2021

Atmospheric Chemistry and Physics Discussions

jump reported from several previously numerical studies in the northeastern coast of Korea (Kim and Cheong, 2006; Jang and Chun, 2008; Lee and In, 2009; Lee et al., 2020). The stronger streamwise velocity extended from the upper layers to the downslope of the TMR (exceeding ~36 m s^{-1}) coincident with downdraft, which is similar to the downslope windstorm that contributed to the increased temperature via adiabatic warming on the slope. Along with this, surface velocity was intensified exceeding ~12 m s^{-1} near the surface at the GWW site associated with the downslope wind. Note that the magnitudes of streamwise velocity are consistent with the fluctuation of the surface wind speed observed from the AWS (wind speed in Fig. 6). The result from this LDAPS analysis suggested that the downslope wind dominated the acceleration of wind speed in the lee side of the TMR.

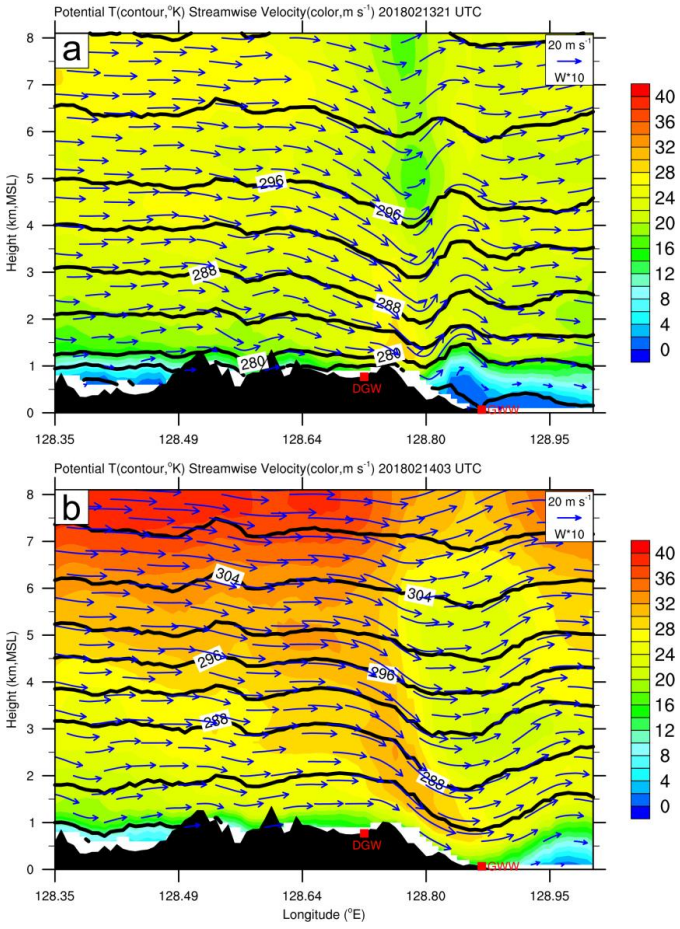

https://doi.org/10.5194/acp-2021-100
Preprint. Discussion started: 25 February 2021


Atmospheric Chemistry and Physics Discussions

519 **Figure 10.** Vertical cross section of the LDAPS potential temperature (ºK, contours), streamwise velocity (m s^{-1},
520 color shading), and airflow (vectors) along the black lines in Fig. 9a at (a) 21:00 UTC on 13 Feb. 2018 and (b) 03:00
521 UTC on 14 Feb. 2018. The black shading in the lower portion indicates the topography along the black line in Fig.
522 9.

523 **5 Stronger winds in mountainous area**

524 **5.1 The lidar and AWS observations**

525 The combination of the LPS and HPS provided a large-scale environmental wind favorable
526 for westerly over mountainous area. According to the DGW QVP from observations (Fig. 11a),
527 the wind speed ranged from ~12 to 36 m s^{-1} at the low-level layers (~900 to 1800 m MSL) during
528 12:00 UTC on 13 February to 12:00 UTC on 14 February 2018. After this time period, the wind
529 was decaying so quickly becoming nearly calm associated with the approaching HPS (Fig. 2e).
530 The surface wind fluctuates in the range of 7 m s^{-1} to 12 m s^{-1} with the periodicity of 6h at the
531 DGW site, similar to the pattern in the lidar QVP (Fig. 11b). These characteristics were quite
532 different from the AWS and lidar observations in the lee side of mountains (for example GWW
533 site). Unlike the coastal site, the strong wind can sustain for a day in the mountainous area. In
534 particular, there was persistent westerly at the entire altitude in the mountainous area (i.e., DGW
535 site). However, the wind direction was quite variable from southerly to westerly at the lee side of
536 the mountainous area (GWU or GWW site). Significant strong winds were measured at the DGW
537 site above 1000 m MSL on 13 February (Fig. 11), wind was weak at the GWU site (Fig. 6).
538 Although the wind was getting stronger at the GWU and GWW sites on ~02:00 UTC on 14
539 February, the low-level or surface winds are getting slightly weaker at the DGW site. This trend
540 is consistent with the wind fields from the sounding observations at the DGW site (Figs. 4a and
541 4b).

542 The AWS observations at the DGW site demonstrated sustained strong westerlies (~10 m s^{-1})

https://doi.org/10.5194/acp-2021-100
Preprint. Discussion started: 25 February 2021


Atmospheric Chemistry and Physics Discussions

with periodic fluctuation from 12:00 UTC on 13 February to 12:00 UTC on 14 February 2018 (Fig. 11b). Although the wind speed fluctuated periodically, no periodicity was shown in the perturbation pressure and perturbation temperature. Instead, the perturbation pressure monotonically dropped from 3 hPa at 12:00 UTC on 13 February to -2 hPa at 05:00 UTC on 14 February and then increased to 1 hPa at 12:00 UTC on 14 February 2018. The perturbation temperature showed nearly opposite trend of the perturbation pressure. The perturbation temperature was nearly steady until 22:00 UTC and then increased to 4.5 ºC at 07:00UTC on 14 February 2018. Although the movement of LPS affected the changes of the surface perturbation pressure and temperature at the DGW site, the changes of the wind speed had no clear relation with the surface pressure and temperature.

https://doi.org/10.5194/acp-2021-100
Preprint. Discussion started: 25 February 2021

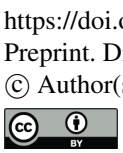

Atmospheric Chemistry and Physics Discussions

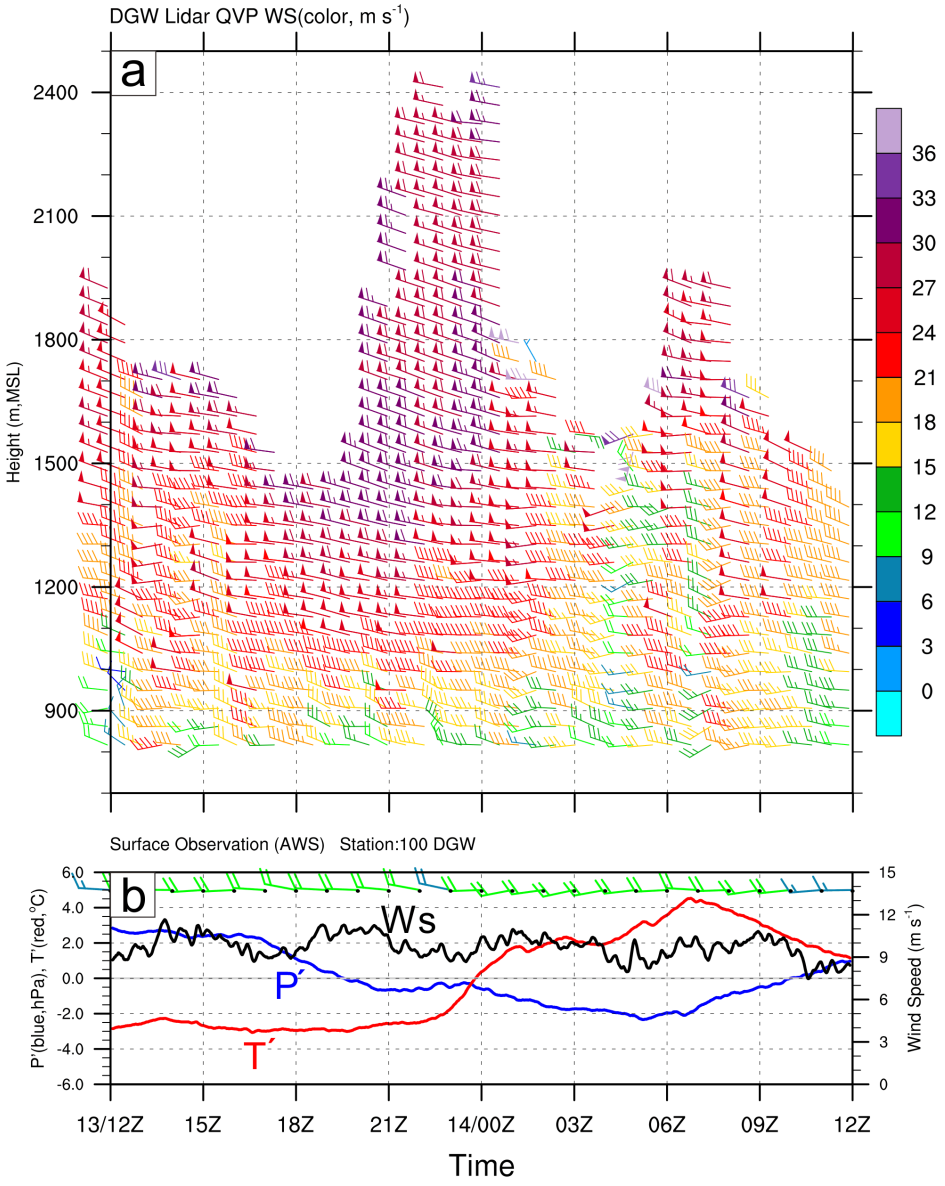

Figure 11. (a) Time series of QVP (Quasi-Vertical profile) from lidar observations at DGW site from 12:00 UTC on 13 Feb. to 12:00 UTC on 14 Feb. 2018. A full wind barb corresponds to 5 m s^{-1}; a half barb corresponds to 2.5 m s^{-1} and the color indicates the wind speed correspond to bar. (b) Time series of the horizontal winds (wind barbs), wind speed (m s^{-1}, black line), perturbation pressure (hPa, P', blue line), and perturbation temperature (ºC, T', red line) observed from the AWS at DGW site.

https://doi.org/10.5194/acp-2021-100
Preprint. Discussion started: 25 February 2021


Atmospheric Chemistry and Physics Discussions

559 **5.2 Possible mechanism of strong wind in mountainous area**

560 To document the possible mechanisms about sustained strong wind occurring at DGW site
561 over the mountainous area, difference of temperature and pressure were analyzed in detail.
562 Similar to the DGW and GWW sites in Fig. 7, an upstream surface station (YPO site in Fig. 1b)
563 was selected to calculate the temperature and pressure differences with the DGW site. Figure 12a
564 reveals that the fluctuation of pressure differences (blue line in Fig. 12a) had an almost out of
565 phase with the fluctuations in wind speed (black line in Fig. 12a) at the DGW site. Furthermore,
566 the wind speed was gently decreasing with periodicity (wavelength of about 6h).This result
567 provided a clue that the pressure gradient likely dominated the wind speed in this local area.
568 Compared to the lee side of the mountains at the GWW site (Fig. 7), negative values of the
569 temperature differences (minimum −1.3 ºC) were calculated in the mountainous area and even
570 became smaller (−0.5 ºC) after 12:00 UTC on 14 February. Thus, the differences of pressure
571 seemed to affect the wind speed patterns, and the fluctuation of wind speed did less relate to
572 differences of temperature between these two sites. Note that the estimated values of Team B in
573 eq.(11) are revealed significant different from observed perturbation pressure at the DGW site
574 (between ~1 hPa and 2 hPa) during entire period, this result also indicated that the fluctuation of
575 pressure is more related to nonhydrostatic effects [Term A in eq. (11)] but sub-cloud
576 warming/cooling (not show). The periodic characteristic of the surface wind may have linked to
577 nonlinear dynamic such as gap flow and gravity wave mechanisms (Shun et al., 2003).
578 The acceleration of wind speed at the DGW site can also be estimated by equation (10). Most
579 of the estimated Term A and wind speed were also in a good agreement except for the short time
580 period (Fig. 12b). Basically, the wind speed was increasing (decreasing) when estimated
581 acceleration (Term A) is positive (negative). To understand the main contributor that dominates
582 such local strong winds in this area, a detailed budget analysis of the momentum equation was
583 performed (Fig. 12c). The PGF (Term C) was the most important factor for the estimated

https://doi.org/10.5194/acp-2021-100
Preprint. Discussion started: 25 February 2021

Atmospheric Chemistry and Physics Discussions

584 acceleration, which means that the PGF could possibly determine the changes of the wind speed
585 at the DGW site. The advective acceleration was relatively small. The Coriolis force and friction
586 had no clear impacts on the acceleration (Term A).

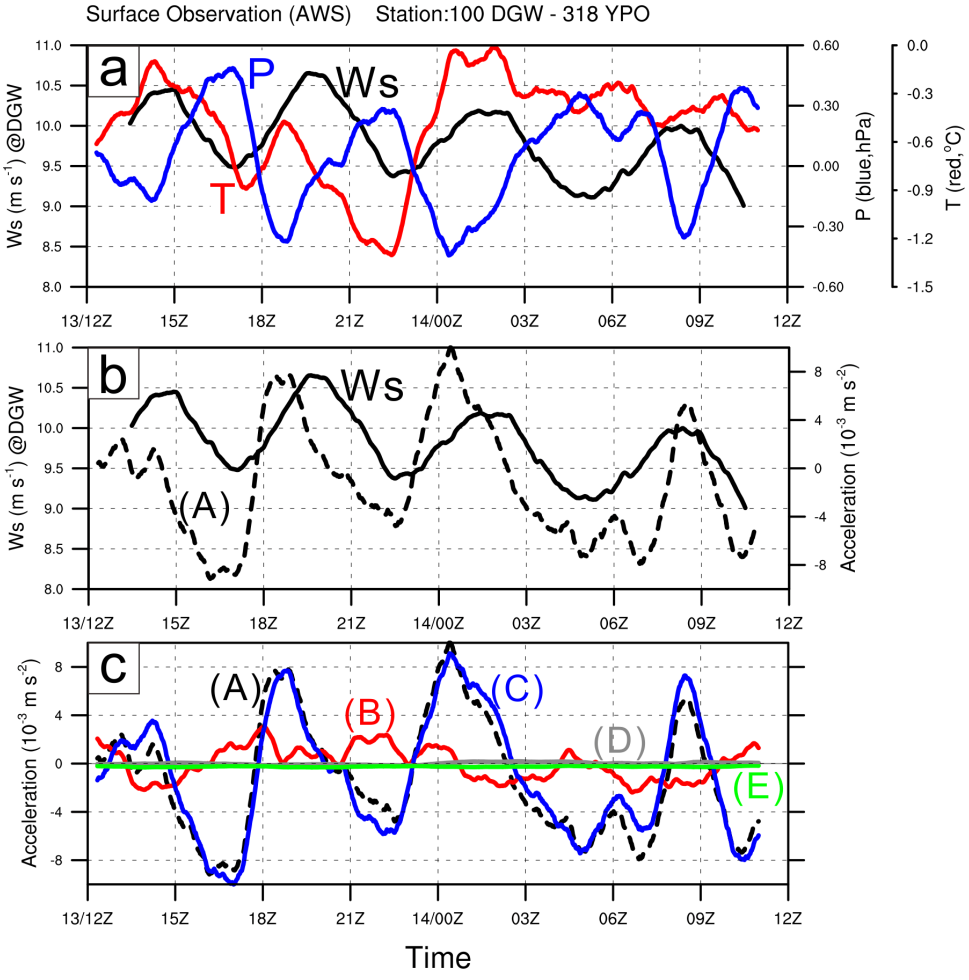

587
588 **Figure 12.** (a) Time series of wind speed (m s^{-1}, black line) observed from the AWS at DGW site, and the differences
589 of sea level pressure (hPa, blue line), temperature (ºC, red line) between the DGW and YPO sites from 12:00 UTC
590 on 13 Feb. to 12:00 UTC on 14 Feb. 2018. (b) Time series of the u component acceleration (10^{-3} m s^{-2}, Term A,
591 black dashed line) estimated from the horizontal momentum equation [eq. (10)] between YPO and DGW sites. (c)
592 Time series of the u component acceleration (Term A, black dashed line), the advective acceleration (Term B, red
593 line), the PGF (Term C, blue line), Coriolis acceleration (Term D, gray line), and friction (Term E, green line).

594 The above results show that PGF is the main factor to accelerate wind speed, but temperature
595 is not a critical factor to change the PGF over the mountainous area. To determine the possible

https://doi.org/10.5194/acp-2021-100
Preprint. Discussion started: 25 February 2021


Atmospheric Chemistry and Physics Discussions

596 factor that contributes into PGF, more detailed analysis of horizontal winds was performed with
597 WISSDOM synthesis. Figure 13 demonstrates the fine-scale wind fields at 800 m MSL (near
598 surface in the studied domain). In this height, a unique topographic feature can be explored as it
599 is composed of a relatively wide (narrow) area in the western (eastern) side along the valley. This
600 channel like feature could be emphasized and was marked by the area between two thin dashed
601 lines in Fig. 13. Four periods (00:00 UTC on 13 February 2018, 00:00 UTC on 14 February,
602 12:00 UTC on 14 February, and 00:00 UTC on 15 February 2018) were selected to investigate
603 the changes of wind patterns in this channel along the valley. The prevailing wind was westerly
604 with a slight deflection near the center of the domain and the eastern side of the valley while the
605 LPS approached Korea (Figs 13a, 13b, and 13c). Nevertheless, a relatively weak wind (~6 m s^{-1})
606 always existed in the center of the domain nearby the MHS lidar site (wide segment of the valley)
607 and a stronger wind (14 m s^{-1}) was observed in the downstream nearby the DGW site (narrow
608 segment of the valley). Wind speed decreased and nearly became calm after the LPS moved away
609 from Korea (Fig. 13d).

https://doi.org/10.5194/acp-2021-100
Preprint. Discussion started: 25 February 2021

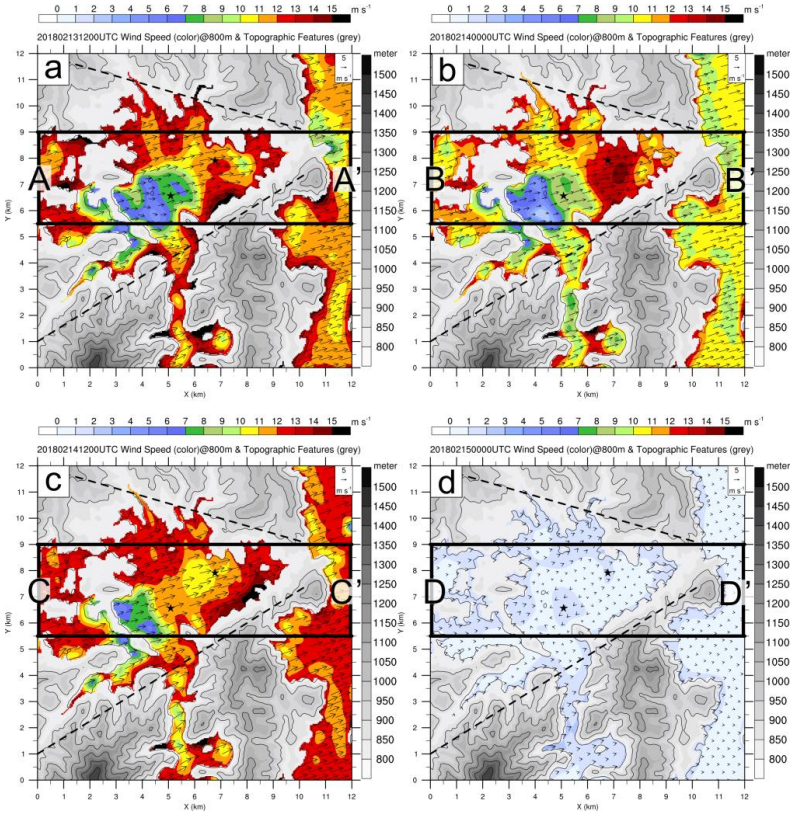

Figure 13. Horizontal distribution of the wind speed (m s^{-1}, color shading) at 800 m (MSL) retrieved in the WISSDOM domain at (a) 00:00 UTC on 13 Feb. 2018, (b), 00:00 UTC on 14 Feb., (c) 12:00 UTC on 14 Feb., and (d) 00:00 UTC on 15 Feb. 2018. The black dashed lines mark the area of the channel to calculate the averaged wind speed and channel width as shown in Fig. 14. The inserted box indicates the averaged area in the vertical cross sections along the valley (A-A'). Topographic features indicated by the gray shading and contours. Locations of the scanning Doppler lidar sites are denoted by asterisks.

To understand the relations between the topography and winds, the average wind speed (colored thick lines in Fig. 14) and the channel width (thick black line in Fig. 14) along the valley at 800 m MSL were calculated in two time periods when the LPS approaches (before 12:00 UTC on 14 February 2018) and leaves (after 12:00 UTC on 14 February 2018). The channel width was around 2 km at x = 0 km to 3 km (western side) and became wider ~5.5 km at x = 3 km to 6.5 km. The channel width then decreased significantly to nearly 0 km at x = 6.5 km to 9.5 km.

When LPS was approaching (average wind speed in red line and range of minimum and

https://doi.org/10.5194/acp-2021-100
Preprint. Discussion started: 25 February 2021

Atmospheric Chemistry and Physics Discussions

624 maximum wind speed in shading in Fig. 14), the average wind speed increased from ~10 m s^{-1}
625 to ~14 m s^{-1}, which was coincident with the changing of channel width from ~5.5 km to 0 km
626 along the valley. The maximum wind speed was larger than 24 m s^{-1} near the narrowest segment
627 of the valley. When LPS was leaving (blue line and shading), the averaged wind speed had a
628 nearly constant strength (~5 m s^{-1}) without obvious changes and no clear relations with the width
629 of the valley. This analysis reveals that the channeling effect may play an important role to
630 dominate the spatial distribution of wind speed with the valley. Furthermore, downstream
631 acceleration in the narrow segment of valley could be more significant with strong upstream
632 winds.

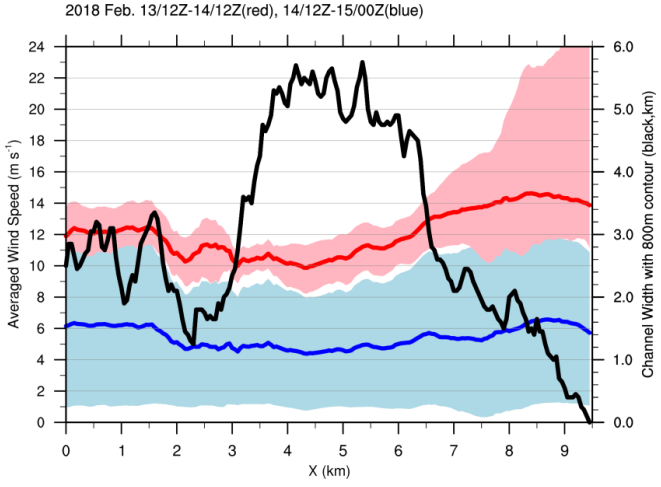

633

634 **Figure 14.** Averaged wind speed and its range along the valley corresponding to the area indicated by the dashed
635 lines in Fig. 13 at two times: 12:00 UTC on 13 Feb. to 12:00 UTC on 14 Feb. (red line and shading) and 12:00 UTC
636 on 14 Feb. to 00:00 UTC on 15 Feb. 2018 (blue line and shading). The red and blue shading show the maximum and
637 minimum values along the valley for the two times. Averaged channel width along the valley was plotted by a thick
638 black line.

639 Figure 15 shows the mean vertical structures of wind speed, airflow, and topographic features
640 from each cross section along the boxes in Fig. 13. The boxes were set on our main focus area
641 from wider to narrow segments along the valley and parallel with the environmental wind
642 direction (westerly). These analyses allow us to investigate detailed airflow features from near

https://doi.org/10.5194/acp-2021-100
Preprint. Discussion started: 25 February 2021

Atmospheric Chemistry and Physics Discussions

643 the surface to higher altitudes and their interactions with topography. The four time periods were
644 12:00 UTC on 13 February 2018, 00:00 UTC and 12:00 UTC on 14 February, and 00:00 UTC
645 on 15 February 2018. The mean vertical structures in the first three periods (when the LPS
646 approaching) revealed similar characteristics that the uniform and stronger westerly winds (larger
647 than ~18 m s^{-1}) were above the layers higher than 1 km MSL. In contrast, the airflow had more
648 significant variances near the surface layers. In the layers below 1 km MSL, the westerly winds
649 were lifted on the upslope and become downdraft behind the mountain crests. The wind speed
650 was quite weak (strong) near the MHS (DGW) site, which is coincident with the relatively wider
651 (narrow) segment in the valley on the three time periods. In particular, the high wind speed area
652 was only presented between x = ~6.5 km and 9.5 km (i.e., the narrowest segment of the valley).
653 The winds became more uniform and weaker in the upper layers and near the surface when the
654 LPS moved away from Korea at 00:00 UTC on 15 February 2018 (Fig. 15d).

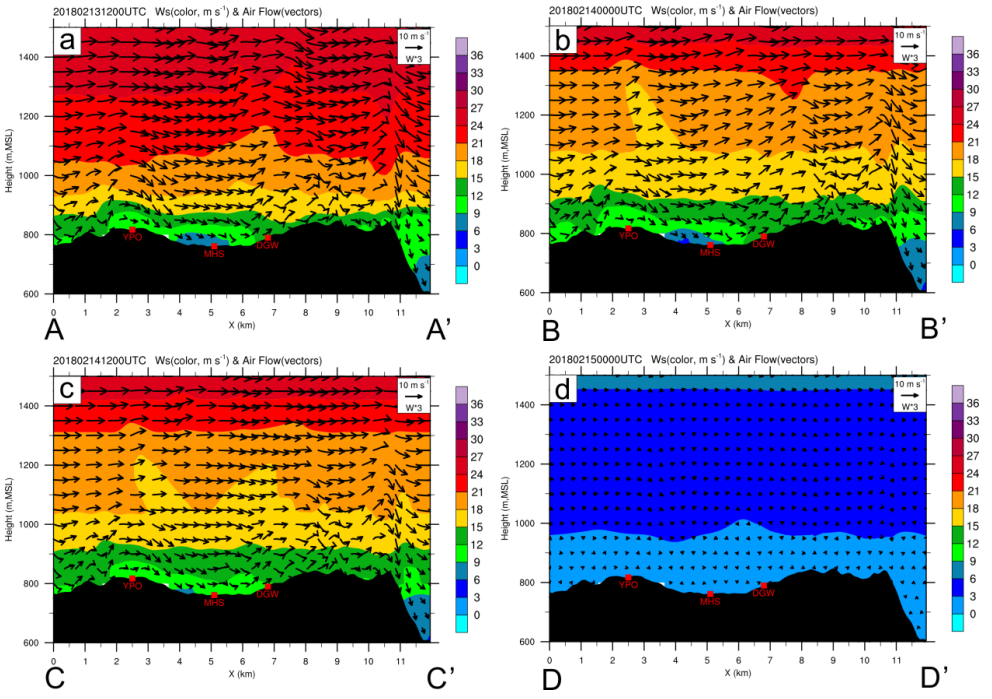

655
656

657 **Figure 15.** Averaged vertical cross section of the WISSDOM-derived wind speed (m s^{-1}, color shading) and wind
658 vectors (combined cross barrier flow and threefold vertical velocity) at four time periods (a) 12:00 UTC on 13 Feb.
659 2018, (b) 00:00 UTC on 14 Feb. 2018, (c) 12:00 UTC on 14 Feb. 2018, and (d) 00:00 UTC on 15 Feb. 2018. The

https://doi.org/10.5194/acp-2021-100
Preprint. Discussion started: 25 February 2021


Atmospheric Chemistry and Physics Discussions

area of the cross section is shown in the black box in Fig. 13. The black shading in the lower portion indicates the topography along the box.

Because the winds manifested clear variations only near the surface layers, the mean vertical structures of wind speed and directions could be further averaged just below 1 km MSL. Fig. 16 shows the continuous time series of averaged wind field during the entire period with the same x axis in Fig. 15. Results demonstrate that the winds near the surface layers were accelerated in the narrow segment between x = ~6.5 km and 9.5 km for strong enough upstream winds (before 00:00 UTC on 14 February). This characteristic is similar to the gap wind or channeling effect from the previous simulation and observational studies (Overland and Walter, 1981; Neiman et al., 2006; Heinemann, 2018). Consequently, a relatively weak channeling effect induced weaker winds in the narrow segment of valley during 00:00–15:00 UTC on 14 February 2018 because the environmental winds from upstream became weaker. Finally, the channeling effect was no longer exiting when the upstream winds became calm after 15:00 UTC. The wind would possibly accelerate when it blows from wider to narrow segments of the valley due to PGF as it is related to the Bernoulli's Law, i.e., the pressure would reduce when the flow speed is increased and vice versa. Observational analysis reveals a relatively low pressure in the narrow segment of valley and thus, PGF would locally dominate the airflow accelerating over the mountainous area.

https://doi.org/10.5194/acp-2021-100
Preprint. Discussion started: 25 February 2021

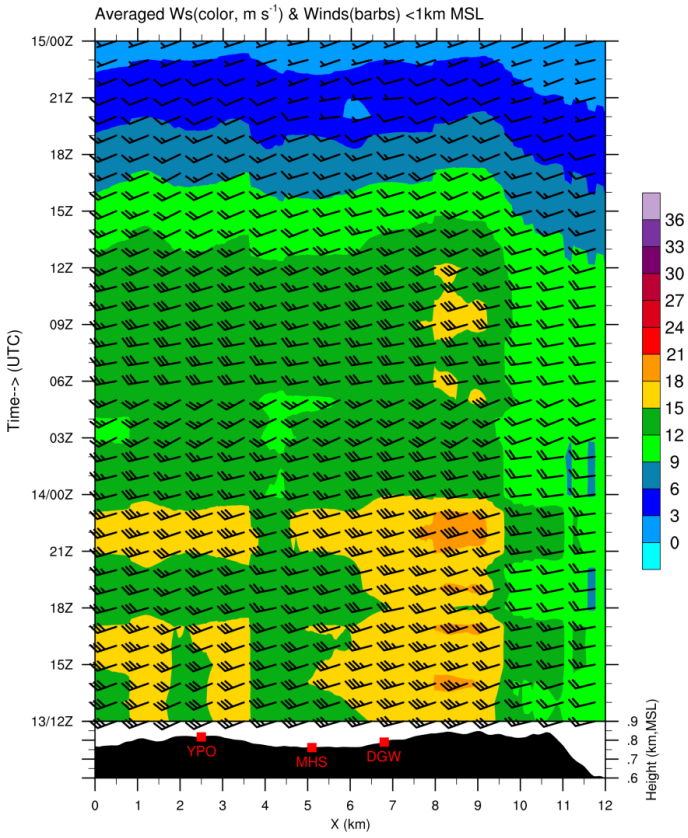

Figure 16. Temporal variation of the averaged wind speed (m s^{-1}, color shading) and the horizontal winds (wind barbs) from WISSDOM derived in the valley from 00:00 UTC 13 Feb. on 13 to 00:00 UTC on 15 Feb. 2018. The low-level winds (below 1 km MSL) within the black boxes in Fig. 15 were averaged in a direction normal to the orientation of the boxes. The black shading in the lower portion indicates the averaged topography along the boxes.

6. Conclusion

This study uses Doppler lidars, wind profiler, soundings, and surface observations to examine a strong downslope wind event during the ICE-POP 2018. Detailed characteristics of wind fields and possible mechanisms were explored during the passage of a low-pressure system (LPS) over the northern part of the Korea Peninsula on 13–15 February 2018. Although the wind speed is generally increased in South Korea when the LPS is approaching, it comprised of more significant increasing trend along the downslope and in the lee side of the TMR (Taebeak

https://doi.org/10.5194/acp-2021-100
Preprint. Discussion started: 25 February 2021


Atmospheric Chemistry and Physics Discussions

689 Mountain Range). The wind speed has no obvious changes but are persistently strong over the
690 TMR. Conspicuous gradient of linear trend of the wind speed only existed between the
691 mountainous areas and in the lee side areas. Moreover, the wind speed shows a decreasing trend
692 synchronously after the LPS moves away from Korea.

693 From the sounding observations, low-level environmental winds revealed high variability
694 from the mountainous area to the lee side of the mountains. The wind direction is comprised of
695 most westerly associated with the LPS and the wind speed are sustainedly strong (~10 m s^{-1}) at
696 the DGW site (i.e., mountainous area) during the research period. However, the wind speed at
697 the lee side (GWW) clearly changed from being relatively weak to a stronger one. The winds
698 then become nearly calm both in the mountainous or lee side areas after the LPS moved away
699 from the Korean peninsula. In addition, upstream inversion layers (at ~850 hPa level) were also
700 detected by sounding observations at the DGW site while the strong wind occurred in the lee side
701 of the mountains.

702 In the lee side of the mountains, the surface wind speed has dramatically increased (from ~3
703 to 12 m s^{-1}) at the GWW site during the research period. The surface temperature (pressure)
704 perturbation is also changed to positive (negative) values and showed significant time lag with
705 wind speed change. The sea level pressure and temperature differences between the mountainous
706 station at the DGW and the lee side station at the GWW demonstrate that the wind speed is
707 suddenly raised with increasing temperature (exceeded ~8.5ºC) and decreasing pressure (from −1
708 hPa to −4 hPa). The estimated wind accelerations [Term A in eq. (10)] are in good agreement
709 with the observed wind speed, which are mainly contributed by the PGF [Term C in eq. (10)].
710 The negative surface perturbation pressure at the GWW site has nearly the same magnitude with
711 the estimated surface perturbation pressure from the integration of the vertical momentum
712 equation. The fluctuation of surface perturbation pressure is mainly dominated by the sub-cloud
713 warming/cooling [i.e., Term B in eq. (11)]. Results indicate that the adiabatic warming plays an
714 important role to reduce the surface pressure and the winds are accelerated by PGF in the lee side

https://doi.org/10.5194/acp-2021-100
Preprint. Discussion started: 25 February 2021


Atmospheric Chemistry and Physics Discussions

of the TMR. Furthermore, the downslope winds were also dominated by the stronger wind occurring along the lee side based on the LDAPS analysis. The development of the strong downslope wind is highly related to the mountain wave and hydraulic jump.

In the mountainous area, persistent surface strong wind (with the fluctuation of 4.5 m s^{-1}) was observed at the DGW site when the LPS was approaching (leaving). The surface wind has no clear relationship with the surface perturbation pressure and perturbation temperature. However, the sea level pressure differences between the upstream station YPO and DGW show similar amplitudes (out of phase) in the fluctuation of surface wind speed. In contrast, the temperature differences are small (between −0.5ºC and 1.2 ºC) with no clear relations with the fluctuation of surface wind at the DGW site. Although the temperature has no clear relation with the strong wind, estimated wind accelerations [Term A in eq. (10)] results are in good agreement with the observed surface wind speed. It means that the PGF is still the main contributor for the wind acceleration at the DGW site. The 3D winds derived from WISSDOM synthesis also reveal that the wind speed at the DGW site (narrow segment in the valley) is always stronger than the YPO site (wider segment in the valley) when the LPS was approaching. Thus, the channeling effect is possible mechanism to dominate the wind acceleration in the mountainous area.

In this study, the observational evidence shows that the different mechanisms are important references to determine the strength and persistence of the orographically strong winds in the same underlaying LPS under fine weather condition. In the future, high-resolution numerical modeling analysis will be performed for all strong wind events during the ICE-POP 2018, because the detailed thermodynamic information was desired to give more complete descriptions about the distribution of potential temperature across the mountainous area. The kinematic and thermodynamic information from the simulations will be important indicators to further investigate the existing of mountain wave, included the hydraulic jump, wave breaking, and partial reflection for the generation of the downslope windstorm. More cases will be included to provide comprehensive explanations of the strong downslope wind in the northeastern

https://doi.org/10.5194/acp-2021-100
Preprint. Discussion started: 25 February 2021


Atmospheric Chemistry and Physics Discussions

741 mountainous part of South Korea. More importantly, we aim to extend our understanding on the
742 variability of winds around the terrain in a very fine-scale even at different seasons.

743

744 *Author contributions.* This work was made possible by contribution from all authors.
745 Conceptualization, CLT, GWL, JHK ; methodology, CLT, YCL, YHL, JHK, and KK; software,
746 CLT, YHL, and KK; validation, KK, YHL, and GWL; formal analysis, CLT, and JHK;
747 investigation, CLT, GWL, and YHL; writing—original draft preparation, CLT; writing—review
748 and editing, GWL, JHK, YCL and YHL; visualization, CLT; supervision, GWL, and YHL;
749 funding acquisition, GWL, YHL, and JHK. All authors have read and agreed to the published
750 version of the manuscript.
751
752 *Competing interests.* The authors declare that they have no conflict of interest.
753
754 *Special issue statement.* This article is part of the special issue "Winter weather research in
755 complex terrain during ICE-POP 2018 (International Collaborative Experiments for
756 PyeongChang 2018 Olympic and Paralympic winter games) (ACP/AMT/GMD inter-journal SI)".
757 It is not associated with a conference.
758
759 *Acknowledgments.* This work was supported by Civil-Military Technology Cooperation Program
760 funded by the Korea Meteorological Administration and Defense Acquisition Program
761 Administration. No. 17-CM-SS-23, KMA2017-04210, [Project Name : Development of fusion
762 technology for Radar wind profiler] and was funded by the Korea Meteorological Administration
763 Research and Development Program under Grant KMI2020-00910. The authors greatly
764 appreciate the participants in the World Weather Research Programme Research Development
765 Project and Forecast Demonstration Project, International Collaborative Experiments for
766 Pyeongchang 2018 Olympic and Paralympic winter games (ICE-POP 2018) hosted by Korea
767 Meteorological Administration (KMA). The Doppler lidars were deployed by the National
768 Institute of Meteorological Sciences (NIMS), KMA and Environment Climate Change Canada
769 (ECCC). We would like to thank many researchers and students (Byung-Chul Choi, Kwang-Deuk
770 Ahn, Namwon Kim, and Seung-bo Choi at KMA, and Choeng-lyong Lee, Daejin Yeom, Kyuhee
771 Shin, DaeHyung Lee, Su-jeong Cho, SeungWoo Baek, Hong-Mok Park, Geunsu Lyu, Eunbi
772 Jeong, Heesang Yoo, Youn Choi, Bo-Young Ye, and Soohyun Kwon at Kyungpook National
773 University) who collected data during the ICE-POP 2018 period.
774

https://doi.org/10.5194/acp-2021-100
Preprint. Discussion started: 25 February 2021

Atmospheric Chemistry and Physics Discussions

775 **References**
776
777 Afanasyev, Y. D., and Peltier, W. R.: The Three-Dimensionalization of Stratified Flow over Two-
778 Dimensional Topography. *J. Atmos. Sci.*, **55**, 19–39, https://doi.org/10.1175/1520-
779 0469(1998)055<0019:TTDOSF>2.0.CO;2, 1998.
780 Cao, Y., and Fovell, R. G.: Downslope Windstorms of San Diego County. Part I: A Case
781 Study. *Mon. Wea. Rev.*, **144**, 529–552, https://doi.org/10.1175/MWR-D-15-0147.1, 2016.
782 Chou, C., Chiang, J., Lan, C., Chung, C., Liao, Y., and Lee, C.: Increase in the range between
783 wet and dry season precipitation. *Nature Geosci.* **6,** 263–267,
784 https://doi.org/10.1038/ngeo1744, 2013.
785 Clark, T. L., Hall, W. D., Kerr, R. M., Middleton, D., Radke, L., Ralph, F. M., Neiman, P. J., and
786 Levinson, D.: Origins of Aircraft-Damaging Clear-Air Turbulence during the 9 December
787 1992 Colorado Downslope Windstorm: Numerical Simulations and Comparison with
788 Observations. *J. Atmos. Sci.*, **57**, 1105–1131,
789 https://doi.org/10.1175/1520-0469(2000)057<1105:OOADCA>2.0.CO;2, 2000.
790 Colle, B. A., and Mass, C. F.: High-Resolution Observations and Numerical Simulations of
791 Easterly Gap Flow through the Strait of Juan de Fuca on 9–10 December 1995. *Mon. Wea.*
792 *Rev.*, **128**, 2398–2422,
793 https://doi.org/10.1175/15200493(2000)128<2398:HROANS>2.0.CO;2, 2000.
794 Durran, D. R.: Mountain waves and downslope winds. In Atmospheric Processes over Complex
795 Terrain. *Meteorological Monographs; American Meteorological Society*, Boston, MA,
796 USA, **23**, pp. 59–81, 1990.
797 Epifanio, C. C., and Qian, T.: Wave–Turbulence Interactions in a Breaking Mountain Wave. *J.*
798 *Atmos. Sci.*, **65**, 3139–3158, https://doi.org/10.1175/2008JAS2517.1, 2008.
799 Finnigan, T. D., Vine, J. A., Jackson, P. L., Allen, S. E., Lawrence, G. A., and Steyn, D. G.:
800 Hydraulic Physical Modeling and Observations of a Severe Gap Wind. *Mon. Wea.*

https://doi.org/10.5194/acp-2021-100
Preprint. Discussion started: 25 February 2021

Rev., **122**, 2677–2687, https://doi.org/10.1175/1520-0493(1994)122<2677:HPMAOO>2.0.CO;2, 1994.

Heinemann, G.: An Aircraft-Based Study of Strong Gap Flows in Nares Strait, Greenland. *Mon. Wea. Rev.*, **146**, 3589–3604, https://doi.org/10.1175/MWR-D-18-0178.1, 2018.

Houghton, D. D., and Kasahara, A.: Nonlinear shallow fluid flow over an isolated ridge. *Commun. Pure Appl. Math.* **21**, 1–23, 1968.

Houze, R. A., Jr.,: Orographic effects on precipitating clouds. *Rev. Geophys.*, **50**, RG1001, doi:10.1029/2011RG000365, 2012,

Jang, W., and Chun, H.: Severe downslope windstorms of Gangneung in the springtime. *Atmosphere*, **18**, 207–224, 2008. (In Korean with English Abstract)

Kawabata, T., Iwai, H., Seko, H., Shoji, Y., Saito, K., Ishii, S., and Mizutani, K.: Cloud-Resolving 4D-Var Assimilation of Doppler Wind Lidar Data on a Meso-Gamma-Scale Convective System. *Mon. Wea. Rev.*, **142**, 4484–4498, https://doi.org/10.1175/MWR-D-13-00362.1, 2014.

Kim, J.-H., and Chung, I.-U.: Study on mechanisms and orographic effect for the springtime downslope windstorm over the Yeongdong region. *Atmosphere*, **16(2)**, 67-83, 2006. (In Korean with English abstract)

Kim, J.-H., and Chun, H.-Y.: A numerical study of clear-air turbulence (CAT) encounters over South Korea on 2 April 2007. *J. Appl. Meteorol. Clim.*, **49**, 2381-2403, https://doi.org/10.1175/2010JAMC2449.1, 2010.

Kim, J.-H., and Chun, H.-Y. : Statistics and possible sources of aviation turbulence over South Korea. *J. Appl. Meteorol. Clim.*, **50**, 311-324, https://doi.org/10.1175/2010JAMC2492.1, 2011.

Kim, J.-H., R. D. Sharman, R. D., Benjamin, S., Brown, J., Park, S.-H. and Klemp, J.: Improvement of Mountain Wave Turbulence Forecast in the NOAA's Rapid Refresh (RAP) Model with Hybrid Vertical Coordinate System, *Weather Forecast*, **34(6)**, 773-

https://doi.org/10.5194/acp-2021-100
Preprint. Discussion started: 25 February 2021

Atmospheric Chemistry and Physics Discussions

780, https://doi.org/10.1175/WAF-D-18-0187.1, 2019

Klemp, J. B., and Lilly, D. R.: The Dynamics of Wave-Induced Downslope Winds. *J. Atmos. Sci.*, **32**, 320–339, https://doi.org/10.1175/1520-0469(1975)032<0320:TDOWID>2.0.CO;2, 1975.

Kühnlein, C., Dörnbrack, A., and Weissmann, M.: High-Resolution Doppler Lidar Observations of Transient Downslope Flows and Rotors. *Mon. Wea. Rev.*, **141**, 3257–3272, https://doi.org/10.1175/MWR-D-12-00260.1, 2013.

Lee, J., and In, S.: A numerical sensitivity experiment of the downslope windstorm over the Yeongdong region in relation to the inversion layer of temperature. *Atmosphere*, **19**, 331–344, 2009. (In Korean with English Abstract)

Lee, J.: A numerical study of the orographic effect of the Taebak mountains on the increase of the downslope wind speed near Gangnung area. *J. Environ. Sci.*, **12**, 1245–1254, 2003. (In Korean with English Abstract)

Lee, J., Seo, J., Baik, J., Park, S., and Han, B.: A Numerical Study of Windstorms in the Lee of the Taebaek Mountains, South Korea: Characteristics and Generation Mechanisms. *Atmosphere*, **11**, 431. https://doi.org/10.3390/atmos11040431, 2020.

Lee, J.- T., Ko, K.- Y., Lee, D.- I., You, C.- H., and Liou, Y.- C.: Enhancement of orographic precipitation in Jeju Island during the passage of Typhoon Khanun (2012), *Atmos. Res.*, **201**, 1245–1254. https://doi.org/10.1016/j.atmosres.2017.10.013, 2017.

Liou, Y., and Chang, Y.: A Variational Multiple–Doppler Radar Three-Dimensional Wind Synthesis Method and Its Impacts on Thermodynamic Retrieval. *Mon. Wea. Rev.*, **137**, 3992–4010, https://doi.org/10.1175/2009MWR2980.1, 2009.

Liou, Y., Chang, S., and Sun, J.: An Application of the Immersed Boundary Method for Recovering the Three-Dimensional Wind Fields over Complex Terrain Using Multiple-Doppler Radar Data. *Mon. Wea. Rev.*, **140**, 1603–1619, https://doi.org/10.1175/MWR-D-11-00151.1, 2012.

https://doi.org/10.5194/acp-2021-100
Preprint. Discussion started: 25 February 2021

Atmospheric Chemistry and Physics Discussions

853 Liou, Y., Chen Wang, T., Tsai, Y., Tang, Y., Lin, P., and Lee, Y.: Structure of precipitating systems
854 over Taiwan's complex terrain during Typhoon Morakot (2009) as revealed by weather
855 radar and rain gauge observations, *J. Hydrology*, **506**, 14-25.
856 https://doi.org/10.1016/j.jhydrol.2012.09.004, 2013.
857 Liou, Y., Chiou, J., Chen, W., and Yu, H.: Improving the Model Convective Storm Quantitative
858 Precipitation Nowcasting by Assimilating State Variables Retrieved from Multiple-
859 Doppler Radar Observations. *Mon. Wea. Rev.*, **142**, 4017–4035,
860 https://doi.org/10.1175/MWR-D-13-00315.1, 2014.
861 Liou, Y., Chen Wang, T., and Huang, P.: The Inland Eyewall Reintensification of Typhoon
862 Fanapi (2010) Documented from an Observational Perspective Using Multiple-Doppler
863 Radar and Surface Measurements. *Mon. Wea. Rev.*, **144**, 241–261,
864 https://doi.org/10.1175/MWR-D-15-0136.1, 2016.
865 Long, R. R.: A Laboratory Model Resembling the "Bishop-Wave" Phenomenon. *Bull. Amer.*
866 *Meteor. Soc.*, **34**, 205–211, https://doi.org/10.1175/1520-0477-34.5.205, 1953.
867 Mass, C. F., and Ovens, D.: The Northern California Wildfires of 8–9 October 2017: The Role
868 of a Major Downslope Wind Event. *Bull. Amer. Meteor. Soc.*, **100**, 235–256,
869 https://doi.org/10.1175/BAMS-D-18-0037.1, 2019.
870 Medina, S., Sukovich, E., and Houze, R. A.: Vertical Structures of Precipitation in Cyclones
871 Crossing the Oregon Cascades. *Mon. Wea. Rev.*, **135**, 3565–3586,
872 https://doi.org/10.1175/MWR3470.1, 2007.
873 Menke, R., Vasiljević, N., Mann, J., and Lundquist, J. K.: Characterization of flow recirculation
874 zones at the Perdigão site using multi-lidar measurements, *Atmos. Chem. Phys.*, **19**, 2713–
875 2723, https://doi.org/10.5194/acp-19-2713-2019, 2019.
876 Neiman, P. J., Ralph, F. M., White, A. B., Parrish, D. D., Holloway, J. S., and Bartels, D. L.: A
877 Multiwinter Analysis of Channeled Flow through a Prominent Gap along the Northern
878 California Coast during CALJET and PACJET. *Mon. Wea. Rev.*, **134**, 1815–

1841, https://doi.org/10.1175/MWR3148.1, 2006.

Overland, J. E., and Walter, B. A.: Gap Winds in the Strait of Juan de Fuca. *Mon. Wea. Rev.*, **109**, 2221–2233,https://doi.org/10.1175/1520-0493(1981)109<2221:GWITSO>2.0.CO;2, 1981.

Panziera, L., and Germann, U.: The relation between airflow and orographic precipitation on the southern side of the Alps as revealed by weather radar. Quart. J. Roy. Meteor. Soc., 136, 222–238, https://doi.org/10.1002/qj.544, 2010.

Park, S.-H., Kim, J.-H., Sharman, R. D., and Klemp, J. B.: Update of Upper-Level Turbulence Forecast by Reducing Unphysical Components of Topography in the Numerical Weather Prediction Model, *Geophys. Res. Lett.*, doi:10.1002/2016GL069446, 2016.

Park, S.-H., Klemp, J., and Kim, J.-H.: Hybrid Mass Coordinate in WRF-ARW and its Impact on Upper-Level Turbulence Forecasting, *Mon. Wea. Rev.* , **147(3)**, 971-985, https://doi.org/10.1175/MWR-D-18-0334.1, 2019.

Reed, T. R.: GAP WINDS OF THE STRAIT OF JUAN DE FUCA. *Mon. Wea. Rev.*, **59**, 373–376, https://doi.org/10.1175/15200493(1931)59<373:GWOTSO>2.0.CO;2, 1931.

Rögnvaldsson, Ó., Bao, J.-W., Ágústsson, H., and Ólafsson, H.: Downslope windstorm in Iceland – WRF/MM5 model comparison, *Atmos. Chem. Phys.*, **11**, 103–120, https://doi.org/10.5194/acp-11-103-2011, 2011.

Ryzhkov, A., Zhang, P., Reeves, H., Kumjian, M., Tschallener, T., Trömel, S., and Simmer, C.: Quasi-Vertical Profiles—A New Way to Look at Polarimetric Radar Data. *J. Atmos. Oceanic Technol.*, **33**, 551–562, https://doi.org/10.1175/JTECH-D-15-0020.1, 2016.

Sharp, J. M.: Columbia Gorge gap flow: Insights from observational analysis and ultra-high-resolution simulation. *Bull. Amer. Meteor. Soc.*, **83**, 1757–1762, https://doi.org/10.1175/BAMS-83-12-1757, 2002.

Shun, C.M., Lau, S.Y., Lee, O.S.M.:Terminal Doppler weather radar observation of atmospheric flow over complex terrain during tropical cyclone passages. *J. Appl. Meteorol.*, **42** ,

https://doi.org/10.5194/acp-2021-100
Preprint. Discussion started: 25 February 2021

Atmospheric Chemistry and Physics Discussions

905 pp. 1697-1710,
906 https://doi.org/10.1175/1520-0450(2003)042%3C1697:TDWROO%3E2.0.CO;2, 2003.
907 Shestakova, A. A., Moiseenko, K. B., and Toropov, P. A.: Hydraulic and Wave Aspects of
908 Novorossiysk Bora. *Pure Appl. Geophys.* **175,** 3741–3757,
909 https://doi.org/10.1007/s00024-018-1802-4, 2018.
910 Smith, C., Hatchett, B., and Kaplan, M.: A surface observation based climatology of Diablo-like
911 winds in California's Wine Country and western Sierra Nevada. *Fire*, **1**, 25,
912 https://doi.org/10.3390/fire1020025, 2018.
913 Smith, R. B.: On Severe Downslope Winds. *J. Atmos. Sci.*, **42**, 2597–
914 2603, https://doi.org/10.1175/1520-0469(1985)042<2597:OSDW>2.0.CO;2, 1985.
915 Stull, R. B.: An Introduction to Boundary Layer Meteorology. Kluwer Academic, 670 pp, 1988.
916 Tollinger, M, Gohm, A., and Jonassen, MO.: Unravelling the March 1972 northwest Greenland
917 windstorm with high-resolution numerical simulations. *Q. J. R. Meteorol.*
918 *Soc*., **145**, 3409– 3431. https://doi.org/10.1002/qj.3627, 2019.
919 Tsai, C., Kim, K., Liou, Y., Lee, G., and Yu, C.: Impacts of Topography on Airflow and
920 Precipitation in the Pyeongchang Area Seen from Multiple-Doppler Radar
921 Observations. *Mon. Wea. Rev.*, **146**, 3401–3424, https://doi.org/10.1175/MWR-D-17-
922 0394.1, 2018.
923 Yu, C., and Cheng L.: Radar Observations of Intense Orographic Precipitation Associated with
924 Typhoon Xangsane (2000). *Mon. Wea. Rev.*, **136**, 497–521,
925 https://doi.org/10.1175/2007MWR2129.1, 2008.
926 Yu, C., and Tsai, C.: Surface Pressure Features of Landfalling Typhoon Rainbands and Their
927 Possible Causes. *J. Atmos. Sci.*, **67**, 2893–2911,
928 https://doi.org/10.1175/2010JAS3312.1, 2010.
929 Yu, C., and Tsai, C.: Structural changes of an outer tropical cyclone rain band encountering the
930 topography of northern Taiwan. *Q. J. R. Meteorol. Soc*, **143**, 1107–1122.

https://doi.org/10.5194/acp-2021-100
Preprint. Discussion started: 25 February 2021

Atmospheric Chemistry and Physics Discussions

931 https://doi.org/10.1002/qj.2994, 2017.

932 Yu, C., Cheng, L., Wu, C., and Tsai, C.: Outer Tropical Cyclone Rainbands Associated with

933 Typhoon Matmo (2014). *Mon. Wea. Rev.*, **148**, 2935–2952,

934 https://doi.org/10.1175/MWR-D-20-0054.1, 2020.